



## Research article

## Integration of transcriptomes analysis with spectral signature of total RNA for generation of affordable remote sensing of Hepatocellular carcinoma in serum clinical specimens

Ibrahim H. Aboughaleb<sup>a</sup>, Marwa Matboli<sup>b</sup>, Sherif M. Shawky<sup>c,d,\*</sup>, Yasser H. El-Sharkawy<sup>a</sup><sup>a</sup> Biomedical Engineering Department, Military Technical College, Cairo, Egypt<sup>b</sup> Medical Biochemistry and Molecular Biology Department, Faculty of Medicine, Ain Shams University, Cairo, Egypt<sup>c</sup> Center of Genomics, Helmy Medical Institute, Zewail City of Science and Technology, Ahmed Zewail Road, October Gardens, 6th of October City, 12578 Giza, Egypt<sup>d</sup> Misr University for Science and Technology, Faculty of Pharmacy, Biochemistry Department, Al-Motamayez District. P.O.BOX: 77, 6th October City, Giza, Egypt

## ARTICLE INFO

## Keywords:

Hepatocellular carcinoma  
 Alpha-fetoprotein  
 Transcriptomes  
 Hyperspectral imaging  
 Spectral signature  
 Remote sensing  
 RNA folding  
 Laser pointer  
 Smartphone CCD camera

## ABSTRACT

Hepatocellular carcinoma (HCC) is a major global health problem with about 841,000 new cases and 782,000 deaths annually, due to lacking early biomarker/s, and centralized diagnosis. Transcriptomes research despite its infancy has proved excellence in its implementation in identifying a coherent specific cancer RNAs differential expression. However, results are sometimes overlapped by other cancer types which negatively affecting specificity, plus the high cost of the equipment used.

Hyperspectral imaging (HSI) is an advanced tool with unique, spectroscopic features, is an emerging tool that has widely been used in cancer detection.

Herein, a pilot study has been performed for HCC diagnosis, by exploiting HIS properties and the analysis of the transcriptome for the development of non-invasive remote HCC sensing.

HSI data cube images of the sera extracted total RNA have been analyzed in HCC, normal subject, liver benign tumor, and chronic HCV with cirrhotic/non-cirrhotic liver groups. Data analyses have revealed a specific spectral signature for all groups and can be easily discriminated; at the computed optimum wavelength. Moreover, we have developed a simple setup based on a commercial laser pointer for sample illumination and a Smartphone CCD camera, with HSI consistent data output. We hypothesized that RNA differential expression and its spatial organization/folding are the key players in the obtained spectral signatures. To the best of our knowledge, we are the first to use HSI for sensing cancer based on total RNA in serum, using a Smartphone CCD camera/laser pointer. The proposed biosensor is simple, rapid (2 min), and affordable with specificity and sensitivity of more than 98% and high accuracy.

## 1. Introduction

Hepatocellular carcinoma is the fourth common cause of cancer globally, with the highest liver-related mortality worldwide. Chronic Hepatitis C, B, and D infections are the leading source of about two-thirds of HCC worldwide [1], besides alcoholic ingestion, dietary toxins as aflatoxins, and non-alcoholic fatty liver [2, 3, 4, 5, 6]. HCC diagnosis is currently achieved through several approaches such as histopathology [7], to distinguish between malignant and benign tumors, through the liver biopsy, which has many drawbacks including invasiveness, high cost, time-consuming, and labor-intensive that, associated with serious complications during and/or after the procedure [8, 9]. Radiologically,

using multiphasic CT scan and MRI according to EASLD and EASL guidelines are being used now for HCC diagnosis [10, 11]. Moreover, Ultrasound and alpha-fetoprotein (AFP) are performed as initial screening and every six months as follow up for the tumor stage [12].

Alfa-feto protein levels in serum biomarker are the golden non-invasive biomarker for HCC detection. As a noninvasive serum biomarker, AFP is notorious for its low accuracy (50%) and sensitivity (79.2%) [13, 14], and cross-reactivity, in addition to, its serum level is elevated in chronic liver disease, and/or patients under certain medications or alcohol abuse. So, the Italian and the American Association for the study of Liver disease role considers an AFP level >200 ng/ml to be demonstrative of HCC [15]. AFP ELISA technique suffers from many

\* Corresponding author.

E-mail address: [sshawky@zewailcity.edu.eg](mailto:sshawky@zewailcity.edu.eg) (S.M. Shawky).

improper features such as low specificity, risk of contamination, and time-consuming [16]. So, there is an urgent need for novel non-invasive serum biomarker/s for enhancing prognosis and early detection of HCC.

HCC progression is a multi-step process, starting from cirrhosis, rejuvenate nodules that provide appropriate microenvironment, leading to conversion of the normal hepatocytes to dysplastic ones, and then to neoplastic lesions; ending with HCC [15]. Moreover, genomic instability due to accumulation of multiple genetic and epigenetic changes/mutations and the acceleration of cell growth, that lead mainly to diversity in gene expression patterns/profiles; accelerates tumor progression ending up with the uncontrolled, rapid growth of less differentiated or undifferentiated cells (Anaplasia); with no chance for complete cell maturation/differentiation, Consequently, a reduction in cell organelles and hence, cancer cell occurs such as the endoplasmic reticulum, and mitochondria. This is could be attributed to the changes occur in cancer cell's nucleus, such as increase in its size, shape and density, and their pores, and the abnormalities in the chromatin and RNA pool [16, 17, 18]. Recently, yang et al, have shown that cancer progression is governed by the presence of numerous altered RNA molecules of different types (coding and non coding) such as up-normal splicing, methylation, alteration in the 3'UTR of mRNAs (variants/alternative polyadenylations), in addition to, numerous heterogeneity in miRNAs and LncRNAs sequences, expression and modifications, which affects significantly the cell dogma RNAs structure, maturation, stability, decay and translation [18]. Moreover, these mutations, differential expression and the interactions with miRNAs, LncRNAs and mRNA are affecting significantly the initiation, and progression of HCC to metastasis [19].

Moreover, compared to the normal cells, the loss of the cancer cell architectural, [incomplete differentiation, small size], and the presence of dysregulated aberrant RNAs, with abundant mutations (different isoforms), lead to up-normal interactions of the RNAs (coding and non-coding), as analyzed by Xu et al [20], using Gene Expression Omnibus for the prediction of the differentially expressed RNAs and their interaction in HCC carcinogenesis. Subsequently, all these factors affecting the spatial organization of the cancer cell, and hence, the folding behavior of its RNAs leading to miss-folded, RNA confirmation, compared to the normal cell, which has compact structure and accurate RNA folding.

**In the same context, Transcriptome is the whole set of all RNA molecules within a cell, and/or group of cells, reflecting the cells' behavior and its response to internal and external factors [21].** Cancer Transcriptome landscape extends beyond protein-mRNA interactions and includes numerous non-coding RNAs [22, 23, 24]. Compared to protein biomarkers, coding and non-coding RNA expression and profiling (circular RNAs, miRNAs, LncRNAs, exosomal RNAs, and mRNA) have shown higher sensitivity and specificity as stable blood-based markers for detecting various types of cancer including HCC [25, 26, 27, 28, 29, 30]. Despite the sensitivity and specificity of qPCR and NGS approaches for transcriptome detection/profiling, they are highly expensive, labor-intensive, and time-consuming; need sophisticated equipment and strenuous data analysis Therefore, liquid biopsies such as, the corresponding circulating RNAs in the blood, extracellular vesicles and circulating tumor cells, are representative to the primary RNAs in the cell of origin in sequence, proteins, and hence RNA folding and/or RNA/p-proteins (nucleoproteins) [31, 32, 33].

Recently, elevated AFP mRNA along with Glypican-3 mRNA has been found in serum extracellular vesicles in HCC patients compared to the control with high positive predictive value [34]. Consequently, modern patterns point to the advancement of panels merging numerous varying RNA markers [35, 36, 37]. Therefore, revealing total RNA profiles for specific cancer diagnosis depending on total RNA profiles/dogma for assertive early diagnosis and/or prognosis of cancer is highly essential [38]. Indeed, Transcriptome techniques provide inclusive molecular information of the different RNAs tested.

Expression profiles for some RNAs have been revealed for all the samples in the study as molecular evidence to the origin (HCC and

normal) of the total extracted RNA from sera specimens in the study. These RNAs are related and linked to HCC pathogenesis and implicated in different HCC molecular pathways carcinogenesis such as transcripts *MCM6 mRNA* and *FOXM1 mRNA*, apoptosis, and immune checkpoint regulation: *STAT1* and *LATI mRNA* and **autophagy: *ATG12 mRNA***. Furthermore, miRNA 23a-3, **miRNA 221-3p**, and **miRNA 106b-3p**, Also, 3 Long non-coding RNAs (lncRNA-WRAP53, LncRNA-CTBP1-AS, and Lnc-RNA-RP11-513115).

Light electromagnetic waves interact with objects generating different optical responses [transmission, absorption, and scattering], according to various object properties such as size, concentration, and spatial organization (shape), in addition to its physical and chemical properties [39]. Light absorption by the molecule/particle leads to the attenuation of the incident light, which is based mainly on the concentration, extinction coefficient of the molecule/s (Figure 1a). In the same context, light scattering leads to the dissemination of light in different directions according to the molecule/s physical & chemical nature (Figure 1b). Moreover, there is a larger illuminated area produced by the light scattered, when applying a reflective white screen behind the molecules solution, in addition to, small intense spot due to attenuated light transmission (Figure 1c).

Hyperspectral imaging (HSI) has come out primarily by NASA as a remote sensing approach in Astrology, earth studies [40], and Agriculture [41] for space research, health crops determination, outbreak plant diseases respectively. HSI has been found its way in medicine mainly in the discrimination between cancer and non-cancerous tissues such as gastric tumors, quantitative prostate cancer detection, and breast cancer [42, 43, 44].

HSI data cube image generates a spatial (x, y), and spectral wavelength information along the entire electromagnetic spectrum in the range of the used camera, with each pixel, provides a specific spectral signature based on the reflection, transmission, and absorption of electromagnetic radiation for any material under examination [45]. These spectral signatures created by the HSI data cube; precisely used in the identification, characterization, and sorting of different materials including cancer [44, 46, 47, 48].

Herein, a pilot study has been performed, utilizing the Hyperspectral imaging system for the identification of the unique spectral signatures for HCC, benign, cirrhotic, and normal subjects based only on total RNA extracted from sera specimens. This was followed by the selection of the optimum wavelength with the highest discrimination between the above mentioned different groups. Moreover, for the first time, we have exploited the data obtained from HSI, in developing a simple, robust, cost-effective setup consisting of a cheap commercial laser pointer and mobile phone CCD camera; which have been employed in differentiation between the different groups.

## 2. Material and methods

### 2.1. Chemicals and equipment

miRNEasy<sup>®</sup> RNA isolation kit (Cat No./ID: 217184, Qiagen, USA), All the PCR kits and primers were purchased from Qiagen, USA. Ultraspec 1000 ultraviolet (UV)/visible spectrophotometer (Amersham Pharmacia Biotech, Cambridge, England), One Step One Plus<sup>™</sup> System (Applied Biosystems Inc., Foster, CA), Commercial enzyme-linked immunoassay (ELISA) kits Abbott Diagnostics Korea Inc (Giheung-gu, Yongin-si, Korea) for detection. Hepatitis Bs Ag (Cat No > 01FK10W), Abbott Diagnostics Korea Inc. (Giheung-gu, Yongin-si, Korea), were used to test the serum anti-HCV antibody (Manufacture cat No,02FK10), and a quantitative investigation of AFP has been done using commercial ELISA kit (Abcam, Cambridge, MA, Cat. Number (AB1808838).

Hyperspectral camera (SOC710VP Surface Optics, USA), Custom MATLAB application (The Math-Works, Natick, MA, USA), and Lens (Schneider KREUZNACH XENOPLAN 1.4).

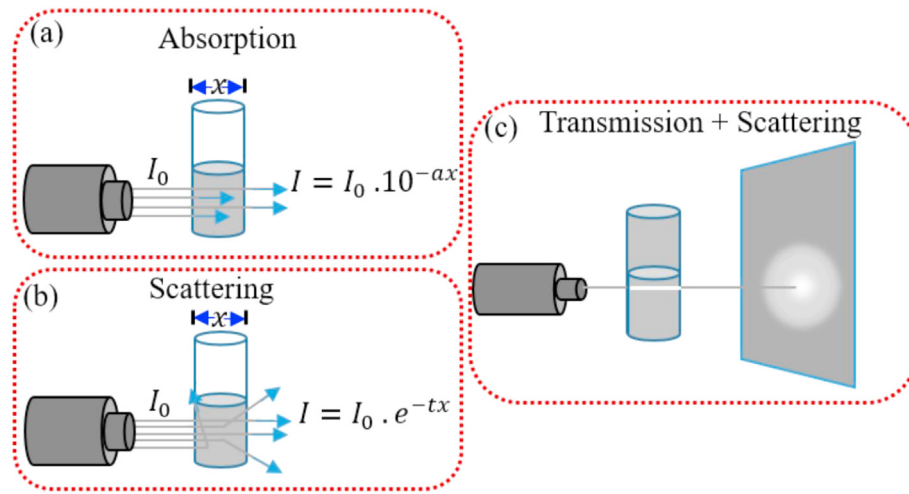


**Figure 1.** Matter and Light interaction: (a) The transmitted light intensity is attenuated by absorption; due to the light absorption of the molecules (b) The transmitted light is exponentially attenuated by scattering; (c) The transmitted and scattered light, could be seen/reflected by a white reflective screen behind the objects/solution under examination. These all effects are based on Beer's Lambert Law.

## 2.2. Sample preparation, viral markers, and serum AFP detection

Written informed consent from all contributors in this study was attained in line with the Declaration of Helsinki. The work was affirmed by the Ethics Committee of Ain Shams Faculty of Medicine, Cairo, Egypt. Venous blood samples were collected from the patients before any therapeutic interventions, including surgery. Patients with a history of other tumors and those receiving radiotherapy or chemotherapy, as well as low quality, extracted RNA samples were excluded from the main study. Serum samples were collected from Clinical Tropical Medicine Department; Ain Shams University Hospital from May 2019 to September 2019. The study includes thirty-six HCC patients, where a diagnosis was performed according to AASLD practical guidelines [12], and classification was consistent with clinical-stage using BCLC [49]. Twenty-four control subjects were enlisted during routine check-ups; in addition to, four HCV chronic infected samples; three samples have liver cirrhosis and one with normal liver, and two patients with a benign liver tumor. Moreover, Serum anti-HCV antibody and hepatitis B surface antigen (HBs Ag) levels and AFP were verified and quantitatively investigated using commercial ELISA kits as mentioned in section 2.1. Total RNA was extracted by miRNEasy® RNA isolation kit from sera samples according to the manufacturer's instructions in 75 ul DNase/RNAase free water. RNA concentration and integrity were assessed using a UV/visible spectrophotometer, with purity ranged from 1.8 to 2. The concentration used for all the samples was 60 ng/ul.

The clinical and demographic descriptions of all the contributors are summarized in Table 1.

## 2.3. The proposed custom optical imaging system

The custom optical imaging system composed of a 10 Watts Halogen lamp (340–1000 nm) as a polychromatic light source for sample illumination, along with a Hyperspectral camera characterized by a 10-degree field of view, spectral and spatial resolution of 4.6875 nm and  $696 \times 520$  pixels respectively; with 128 spectral channels for collecting the transmitted and scattered light of the sample under examination. Moreover, the camera was incorporated with a 35 mm lens of focal length covering 400–1000 nm spectral ranges, the scheme of the system is shown in [Figure 2a], and a photo of the real setup is illustrated in [Figure 2b]. The data has been acquired as a 3D dimension cube-image, where (X & Y) representing the image spatial dimensions; while the third dimension depicting wavelengths.

## 2.4. Spectral cube image processing

Before processing the captured Hyper Spectral (HS) image, the artifacts and electronic noise impacts are wiped out for the obtained image data standardization. So, white equalization and dark current measurements were utilized to acquire relative reflectance from the HS image. The dark cube was captured by covering the HS camera with the lens cap provided with the camera; while the white reference image has been obtained by placing a white sheet (*made of a material that reflects 99% of the incoming radiation*) at the same location and conditions of the specimens. Thus, the information from the dark image and white balance estimations were utilized for the image calibration as shown in Eq. (1):

$$I_{C(\theta)} = \frac{I_{m(\theta)} - I_{d(\theta)}}{I_{w(\theta)} - I_{d(\theta)}} \times 100\% \quad (1)$$

$I_{C(\theta)}$  is the calibrated image,  $I_{m(\theta)}$  is the captured image,  $I_{d(\theta)}$  is the acquired dark image with the lens covered with the cap, and  $I_{w(\theta)}$  is the acquired image when using the white reference.

Custom MATLAB algorithms were used for processing the image data cube. For noise removal and image enhancement, a moving average filter (kernel = 5) has been applied to the calibrated spectrum image (50 nm resolution) as demonstrated in Eq. (2).

$$f(x \times y) = \frac{1}{qt} + \sum_{(r \times c) \in W} S(r \times c) \quad (2)$$

Where 'S' is the noisy image,  $f(x \times y)$  is the enhanced image, and 'r' and 'c' for the row and column coordinates respectively, within a window 'W' of size 'q × t' where the process takes place.

### 2.4.1. Column and row mean calculation algorithm

The row and column mean for each spectrum image have been calculated that represents the amount of transmitted and scattered light of each image pixel [Figure 3a]. Each cube image is composed of a multi-dimensional matrix:  $520 \times 696$  pixels  $\times$  128 frames, so the column-mean will be a vector of  $1 \times 696$ , and the row-mean will be a vector of  $520 \times 1$  for each spectral image respectively. A total of 13 vectors have been selected to cover the entire wavelengths (400 nm–1000 nm), with a resolution of 50 nm between each vector for allocating the optimum wavelength/s with the highest difference between the normal and HCC groups [Figure 3b].

**Table 1.** The clinical and demographic descriptions of all the groups included in the study. The samples in bold were not analyzed by the Hyperspectral camera due to the low volume of the RNA provided. AST: Aspartate Aminotransferase; ALT: Alanine Aminotransferase; U/L: Unit per Liter; AFP: Alpha Feto Protein; ng/ml: nanogram per milliliter HCV Abs: Hepatitis C Virus IgG antibodies; HBVsAg: Hepatitis B virus Surface Antigen; BCLC Stage: Barcelona Clinic Liver Cancer Stage; INR: International Normalized Ratio (Prothrombin time).

Sample NO.	Group	Age	Sex	Smoking	Alcohol	AST U/L	ALT U/L	Total bilirubin	Direct bilirubin	Albumin mg/dl	INR	HCV Abs	HBVs Ag	Cirrhosis	BCLC stage	AFP (ng/ml)
H1	HCC	53	male	smoker	Non alcoholic	100.0	63.0	1.5	0.6	2.6	1.4	Pos.	Neg.	Cirrhosis	A6	350
H2	HCC	60	male	smoker	Non alcoholic	58.0	43.0	1.3	0.6	3.2	1.2	Pos.	Neg.	Non-Cirrhosis	A7	130
H3	HCC	60	female	non smoker	Non alcoholic	103.8	73.3	1.5	0.8	2.4	1.5	Pos.	Neg.	Cirrhosis	A8	355
H4	HCC	65	male	non smoker	Non alcoholic	39.0	31.0	1.76	0.9	2.7	1.6	Pos.	Neg.	Cirrhosis	A6	73.8
H5	HCC	60	female	non smoker	Non alcoholic	60.0	32.0	1.0	0.35	2.9	1.3	Pos.	Neg.	Cirrhosis	A2	20
H6	HCC	60	male	smoker	Non alcoholic	128	78	2.4	1.6	4	1.5	Pos.	Neg.	Cirrhosis	A6	138
H7	HCC	60	male	Non smoker	Non alcoholic	137	65	3.4	1.9	3.9	1.6	Neg.	Neg.	Cirrhosis	B7	147
H8	HCC	60	male	smoker	Non alcoholic	260	88	4.5	2.7	2.9	1.6	Neg.	Neg.	Cirrhosis	A6	100.5
H9	HCC	60	male	smoker	Non alcoholic	106	58	2.5	1.6	3	1.3	Neg.	Neg.	Cirrhosis	B8	16.9
H10	HCC	55	female	Non smoker	Non alcoholic	108	57	1.4	0.8	3.3	1.4	Pos.	Neg.	Cirrhosis	B8	16.5
H11	HCC	49	female	smoker	Non alcoholic	26	25	1	0.2	3.4	1.5	Pos.	Neg.	Cirrhosis	A6	4.14
H12	HCC	55	female	Non smoker	Non alcoholic	28	24	1.6	0.4	3.5	1.17	Neg.	Neg.	Cirrhosis	A6	5.1
H13	HCC	58	male	Smoker	Non alcoholic	75	50	2.2	1.2	2	1.7	Pos.	Neg.	Cirrhosis	A5	6.5
H14	HCC	60	male	non smoker	Non alcoholic	32	27	1.9	1.1	4.3	1.08	Pos.	Neg.	Cirrhosis	A5	5.3
H15	HCC	60	male	Smoker	Non alcoholic	60	90	1.2	0.6	4.2	1.4	Pos.	Pos.	Cirrhosis	A5	80
H16	HCC	42	female	non smoker	Non alcoholic	93	63	0.9	0.6	5	1.16	Pos.	Neg.	Cirrhosis	A5	81.86
H17	HCC	50	female	Smoker	Non alcoholic	60	90	1.4	0.8	5	1.6	Pos.	Neg.	Cirrhosis	A5	84
H51	HCC	54	female	non smoker	Non alcoholic	11	35	1.1	0.3	2.4	1.26	Pos.	Neg.	Cirrhosis	B8	170
H19	HCC	53	female	Smoker	Non alcoholic	100	63	2.9	2.1	2.6	1.4	Pos.	Neg.	Cirrhosis	B5	350
H20	HCC	60	male	Smoker	Non alcoholic	58	43	1.3	0.6	3.2	1.2	Pos.	Neg.	Cirrhosis	B5	355
H21	HCC	50	female	non smoker	Non alcoholic	30	18	0.9	0.4	4.1	1.7	Pos.	Neg.	Cirrhosis	A5	4.5
H22	HCC	59	male	smoker	Non alcoholic	32	27	1.3	0.9	4.3	1.12	Pos.	Neg.	Cirrhosis	A5	4.9
H23	HCC	55	female	non smoker	Non alcoholic	25	20	1.3	0.5	3.9	1.05	Pos.	Neg.	Cirrhosis	A5	8.2
H24	HCC	56	female	smoker	Non alcoholic	40	23	0.9	0.4	4.2	1.3	Pos.	Neg.	Cirrhosis	A5	10.5
H25	HCC	60	male	smoker	alcoholic	22	26	1.3	0.4	4.6	1.13	Pos.	Neg.	Non-Cirrhosis	A5	130
H26	HCC	57	male	non smoker	Non alcoholic	24	29	1.2	0.3	4.2	1.09	Pos.	Neg.	Non-Cirrhosis	A5	160
H27	HCC	60	male	smoker	Non alcoholic	24	29	0.99	0.3	3.9	1.05	Pos.	Neg.	Non-Cirrhosis	A5	3.6
H28	HCC	54	female	non smoker	non-alcoholic	22	38	0.8	0.3	3.6	1.01	Pos.	Pos.	Cirrhosis	A5	4.5
H29	HCC	60	male	smoker	non-alcoholic	25	73.3	1.2	0.7	4.5	1.2	Pos.	Pos.	Cirrhosis	A5	8
H30	HCC	65	male	smoker	non-alcoholic	39	19	1.76	0.9	2.7	1.6	Pos.	Neg.	Cirrhosis	B8	1200
H34	HCC	60	male	non smoker	alcoholic	60	70	1	0.35	2.9	1.3	Pos.	Pos.	Cirrhosis	B7	136
H35	HCC	60	male	smoker	Non alcoholic	88	66	1.3	0.5	2.9	1.2	Pos.	Neg.	Cirrhosis	B7	165
H36	HCC	64	male	smoker	Non alcoholic	218	52	3.9	2.2	3.2	1.7	Pos.	Neg.	Cirrhosis	B8	1.6
B7 Benign	Chronic HCV	60	male	non smoker	Non alcoholic	29	11	1.54	0.7	3.6	1.28	Pos.	Pos.	cirrhosis	NA	2.3
B10 Benign	Chronic HCV	55	male	Smoker	Non alcoholic	24	32	2.2	0.6	3.8	1.9	Pos.	Pos.	Non-cirrhosis	NA	2.2
C1	Chronic HCV	60	male	non smoker	Non alcoholic	29	11	1.54	0.7	3.6	1.28	Pos.	Pos.	Cirrhosis	NA	2.3
C2	Chronic HCV	55	male	smoker	Non alcoholic	24	32	2.2	0.6	3.8	1.9	Pos.	Pos.	Non-Cirrhosis	NA	2.2
C3	Chronic HCV	55	female	non smoker	Non alcoholic	30	18	0.5	0.5	4	1.1	Pos.	Pos.	Cirrhosis	NA	3.4
C4	Chronic HCV	50	male	smoker	Non alcoholic	28	18	0.3	0.3	4.2	1	Pos.	Pos.	Cirrhosis	NA	1.8
N1	Normal	50	female	non smoker	Non alcoholic	24.0	22.0	0.923	0.52	3.5	1	Neg.	Neg.	Non-Cirrhosis	NA	7
N2	Normal	52	male	non smoker	Non alcoholic	30.0	19.0	0.85	0.34	4	1.28	Neg.	Neg.	Non-Cirrhosis	NA	13

(continued on next page)

Table 1 (continued)

Sample NO.	Group	Age	Sex	Smoking	Alcohol	AST U/L	ALT U/L	Total bilirubin	Direct bilirubin	Albumin mg/dl	INR	HCV	Abs	HBVs Ag	Cirrhosis	BCLC stage	AFP (ng/ml)
N3	Normal	53	male	non smoker	Non alcoholic	12.0	11.0	1.10	0.7	3.6	0.98	Neg.	Neg.	Non-Cirrhosis	NA	7	
N4	Normal	59	male	smoker	Non alcoholic	29.0	32.0	1.54	0.5	4.3	0.8	Neg.	Neg.	Non-Cirrhosis	NA	39	
N5	Normal	56	female	smoker	Non alcoholic	16.0	20.0	2.2	0.6	5	1.1	Neg.	Neg.	Non-Cirrhosis	NA	59	
N6	Normal	56	female	Non smoker	Non alcoholic	127	17	0.5	0.2	5	0.7	Neg.	Neg.	Non-Cirrhosis	NA	3.1	
N7	Normal	60	male	smoker	Non alcoholic	19	18	0.5	0.2	4	1.1	Neg.	Neg.	Non-Cirrhosis	NA	2.3	
N8	Normal	59	male	non-smoker	Non alcoholic	13	18	0.5	0.3	4.8	0.8	Neg.	Neg.	Non-Cirrhosis	NA	3.6	
N9	Normal	56	female	non smoker	Non alcoholic	17	19	0.3	0.1	4.9	0.9	Neg.	Neg.	Non-Cirrhosis	NA	3	
N10	Normal	56	female	smoker	Non alcoholic	18	18	0.5	0.3	4.8	0.8	Neg.	Neg.	Non-Cirrhosis	NA	2.6	
N11	Normal	60	male	smoker	Non alcoholic	17	18	0.5	0.2	4	1.1	Neg.	Neg.	Non-Cirrhosis	NA	2.9	
N12	Normal	60	male	Non smoker	Non alcoholic	18	19	0.3	0.1	4.9	0.9	Neg.	Neg.	Non-Cirrhosis	NA	1.9	
N13	Normal	58	male	smoker	Non alcoholic	17	13	0.3	0.1	4.9	0.8	Neg.	Neg.	Non-Cirrhosis	NA	1.4	
N14	Normal	50	female	smoker	Non alcoholic	18	17	0.5	0.2	5	0.7	Neg.	Neg.	Non-Cirrhosis	NA	4.1	
N15	Normal	49	female	non smoker	Non alcoholic	18	18	0.5	0.3	4.8	0.8	Neg.	Neg.	Non-Cirrhosis	NA	4.3	
N16	Normal	50	female	smoker	Non alcoholic	19	17	0.5	0.2	5	0.7	Neg.	Neg.	Non-Cirrhosis	NA	3.6	
N17	Normal	45	female	smoker	Non alcoholic	18	18	0.5	0.2	4	1.1	Neg.	Neg.	Non-Cirrhosis	NA	2.4	
N18	Normal	55	female	smoker	Non alcoholic	18	12	0.3	0.2	5.1	0.9	Neg.	Neg.	Non-Cirrhosis	NA	3.2	
N19	Normal	45	female	smoker	Non alcoholic	19	18	0.5	0.2	4	1.1	Neg.	Neg.	Non-Cirrhosis	NA	1.5	
N20	Normal	55	female	non smoker	Non alcoholic	13	18	0.5	0.3	4.8	0.8	Neg.	Neg.	Non-Cirrhosis	NA	2.5	
N21	Normal	45	female	smoker	Non alcoholic	17	19	0.3	0.1	4.9	0.9	Neg.	Neg.	Non-Cirrhosis	NA	2	
N22	Normal	59	male	smoker	Non alcoholic	18	18	0.5	0.3	4.8	0.8	Neg.	Neg.	Non-Cirrhosis	NA	2	
N23	Normal	45	female	smoker	Non alcoholic	17	18	0.5	0.2	4	1.1	Neg.	Neg.	Non-Cirrhosis	NA	1.8	
N24	Normal	61	male	non smoker	Non alcoholic	18	16	0.34	0.1	3.6	1	Neg.	Neg.	Non-Cirrhosis	NA	1,5	

The rows and column of the spectral image I of size M x N is shown in Eq. (3):

$$I = \begin{bmatrix} A_{11} & A_{12} \dots \dots & A_{1N} \\ A_{21} & A_{22} \dots \dots & A_{2N} \\ \vdots & \vdots & \vdots \\ \vdots & \vdots & \vdots \\ A_{M1} & A_{M2} \dots \dots & A_{MN} \end{bmatrix} \tag{3}$$

Where M and N are the number of rows and columns in an image respectively, and A is the pixel value (Corresponds to any value called pixel intensity where the intensity of an image varies with the spatial location of a pixel).

Then, for computing the column-mean and row mean of an image I with size M x N, returns a vector  $\bar{I}_a$  as shown in Eqs. (4) and (5) for column-mean and  $\bar{I}_b$  Eqs. (6) and (7) for the row mean:

$$\bar{I}_N = \frac{1}{M} \left( \sum_{i=1}^M (A_{iN}) \right) = \frac{A_{1N} + A_{2N} + \dots \dots \dots + A_{MN}}{M} \tag{4}$$

$$\bar{I}_a = [\bar{I}_1 \quad \bar{I}_2 \quad \dots \dots \quad \bar{I}_N] \tag{5}$$

$\bar{I}_a$  = the column-mean of the spectrum image I.

$$\bar{I}_M = \frac{1}{N} \left( \sum_{i=1}^N (A_{Mi}) \right) = \frac{A_{M1} + A_{M2} + \dots \dots \dots + A_{MN}}{N} \tag{6}$$

$$\bar{I}_b = [\bar{I}_1 \quad \bar{I}_2 \quad \dots \dots \quad \bar{I}_N] \tag{7}$$

$\bar{I}_b$  = the row-mean of the spectrum image I.

2.4.2. Spectral image column and row root mean square error calculations

The highest spectrum response precise difference between the normal and the HCC groups has been revealed by the calculation of the root-mean-square error (RMSE) as shown in [Figure 3b] and represented by Eqs. (8) and (9).

$$RMSE(\text{column mean}) = \sqrt{\left( \bar{I}_{a(\text{normal})} - \bar{I}_{a(\text{abnormal})} \right)^2} \tag{8}$$

$$RMSE(\text{row mean}) = \sqrt{\left( \bar{I}_{b(\text{normal})} - \bar{I}_{b(\text{abnormal})} \right)^2} \tag{9}$$

Where;  $\bar{I}_a$  = the column-mean of the spectrum image I, and  $\bar{I}_b$  = the row-mean of the spectrum image I.

2.4.3. Spectral signature algorithm for the cube image

After resolving the wavelengths, with the highest RMSE between the two groups, Refining the spectral signature algorithm has been produced by averaging all the 128 frames at 5 nm resolution of the cube image through the entire wavelengths for **rigorously** determine the Spatial mean using Eq. (10).

$$\bar{I} = \left( \frac{1}{N} \sum_{i=1}^N (\bar{I}_i) \right) = \frac{\bar{I}_1 + \bar{I}_2 + \dots \dots \dots + \bar{I}_N}{N} \tag{10}$$

Where: N is the number of rows; while  $\bar{I}$  the column-mean of the spectral image, and  $\bar{I}$  is the spatial mean (the mean of  $\bar{I}$ ).

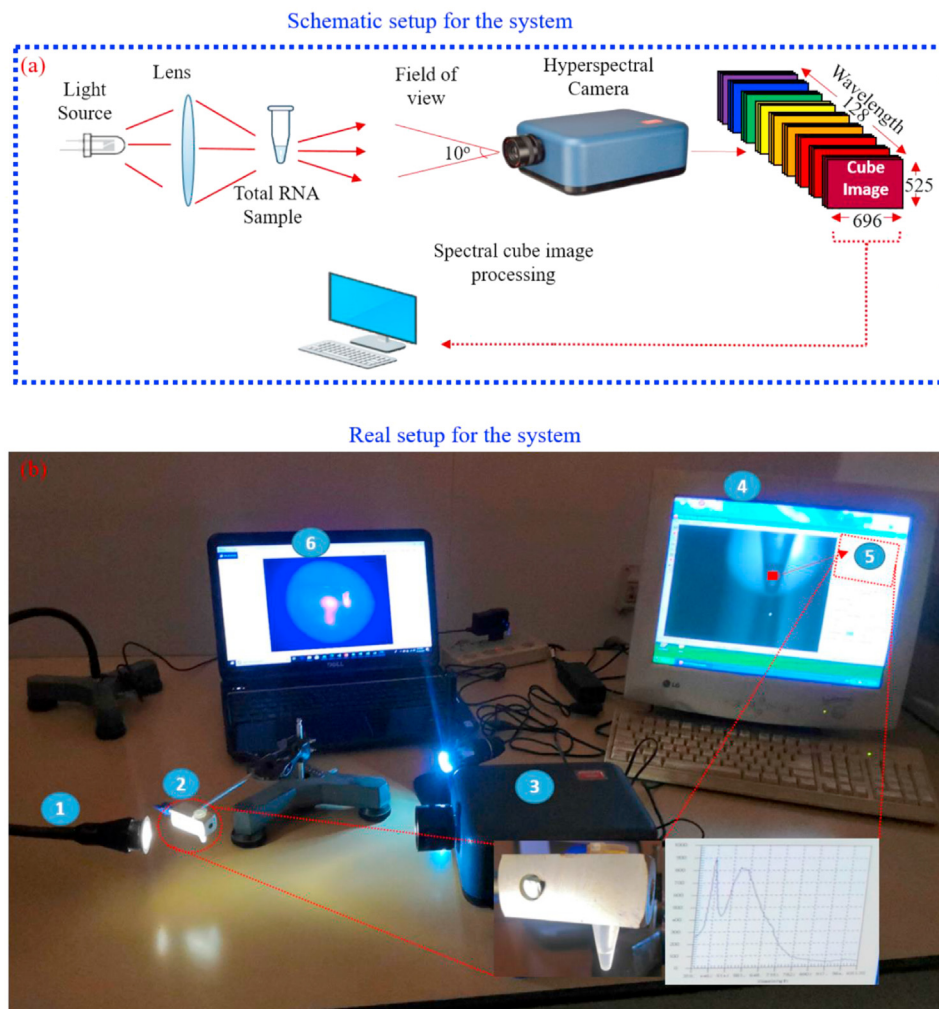


**Figure 2.** Experimental setup schematic/Real representation of the proposed optical imaging system including hardware and software processing. (a) Schematic setup for the system includes a Halogen lamp as a polychromatic light source, a collimated lens, and the tube containing the total RNA extracted from serum. The field of view is  $10^\circ$ , and the Hyperspectral camera captures the image, producing the cube image which is subjected to software processing; (b) Real setup for the system: (1) Polychromatic source light (Halogen lamp, 10 W, 340–1000 nm), (2) The investigated RNA specimen, (3) The HS camera used (Surface Optics, SOC710, USA), (4) Computer with HS camera software for acquiring cube images, (5) A one pixel spectral signature concerning sample under test. (6) Computer with image processing software and data analysis.

#### 2.4.4. Spectral signature normalization and cross-correlation

Amplitude neutralization has been achieved by the normalization of the obtained spectral signature, at the allocated wavelength, between the two groups [Figure 5].

Finally, a cross-correlation matrix has been done for computing the specific spectral signature differences between the different group targets.

#### 2.5. Spectral signature of clinical samples with different criteria

To apply the obtained spectral signature, and measure its specificity and sensitivity, various clinical samples have been analyzed using Hyperspectral camera and analyzed using the above mentioned algorithms. Specimens selection was done not only for HCC and normal samples, but also samples with liver benign tumors, and other with chronic HCV infection 3 cirrhotic and one non-cirrhotic.

#### 2.6. Thermal effect on RNA by hyperspectral camera/laser source

Normal and HCC groups have been subjected to heating at  $80^\circ\text{C}$  for 2 min and then cooled to room temperature for 5 min. Then, Spectral images have been taken by a Hyperspectral camera, illuminated with the selected laser source has  $650\text{nm} \pm 10$  illumination range; which is the determined spectral signature wavelength. Images have been acquired twice before and after heating to elucidate the thermal energy effect on RNA folding behavior and their spectral signatures.

#### 2.7. Real time-PCR (qPCR) quantification of RNA cancer panel

Expression of the selected LncRNAs, miRNAs, and mRNAs in sera samples in the different groups have been done using: RT<sup>2</sup> SYBR Green ROX qPCR (Qiagen, USA) and commercial RT<sup>2</sup> IncRNA qPCR Assay, QuantiTest SYBR® Green qPCR (Qiagen, USA) was used along with the specific primers, and MiScript SYBR® Green qPCR kit with compatible commercial primers respectively. The qPCR was performed according to the manufacturer's protocol of each kit. One Step One Plus™ System (Applied Biosystems Inc., Foster, CA) was used for qPCR reactions. The  $2^{-\Delta\Delta\text{Ct}}$  method was employed for the calculation of the relative quantification of the RNA cancer panel. RNU6 (Hs\_SNORD682.11 MiScript Primer Assay) served as the housekeeping gene for the miRNAs and  $\beta$ -actin (RT<sup>2</sup> IncRNA qPCR Assay for Human ACTB) for lncRNA and mRNA. Also, the raw data were analyzed in comparison with control samples. All the data has been analyzed by using Statistical Package for the Social Sciences (SPSS, Chicago, IL) version 20. The data are shown in Figure 8.

#### 2.8. Commercial laser source and HSI experimental procedures

Herein, the illumination system is composed of a commercial laser pointer ( $650\text{nm} \pm 10$ , max output power  $< 5\text{mW}$ ), and the image was acquired using CCD mobile phone camera, and analyzed using the same algorithms that have been used for HSI.

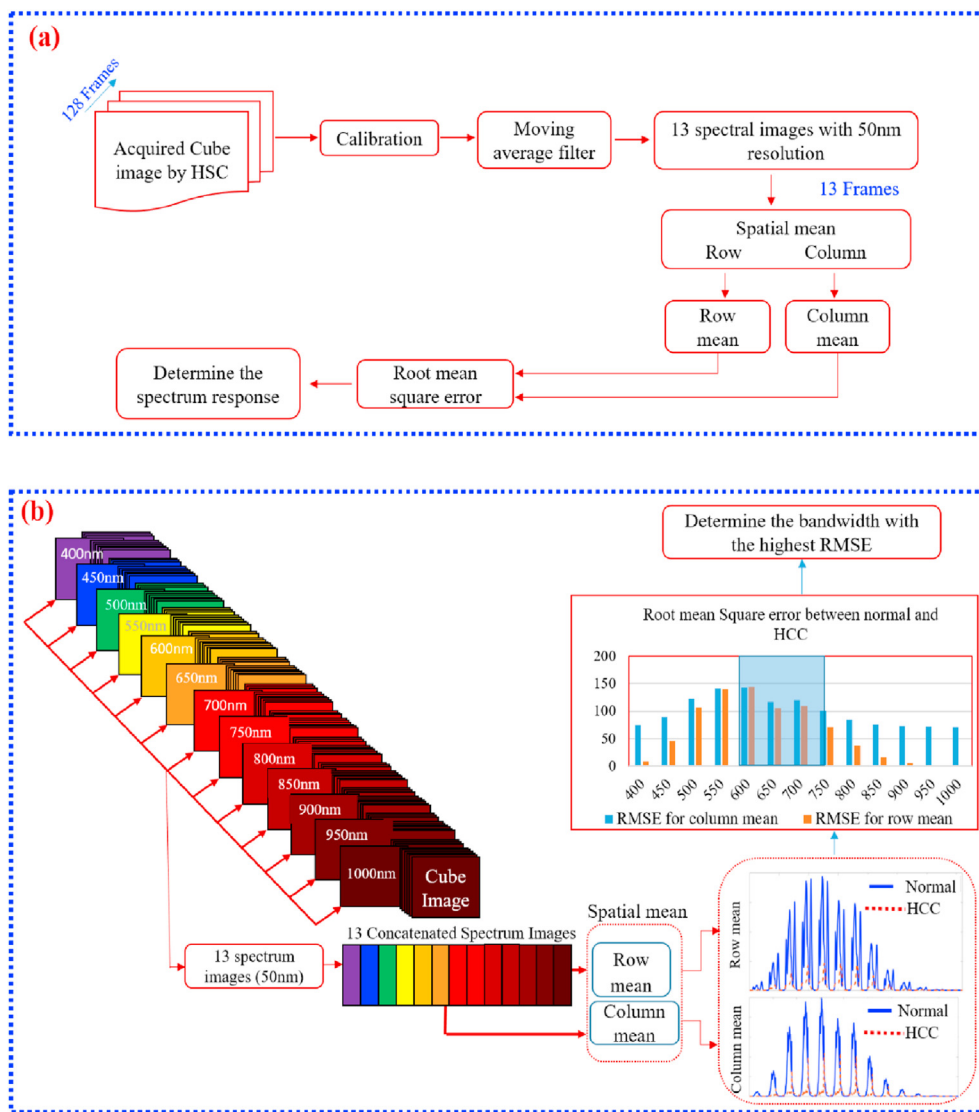


**Figure 3.** The image processing protocol for the Determination of the spectrum response for both the HCC and normal in RNA sera samples. (a) A flowchart for the acquired cube image presenting each step in determining the spectrum responses which starts firstly by acquiring the cube image by the HSC, secondly by cube image calibration for artifacts and electronic noise impacts whipping out, thirdly by noise removal and image enhancement by applying a moving average filter; fourthly by selecting 13 spectrum images that cover the entire wavelength (400:1000nm), with a resolution of 50 nm between each spectral image for allocating the optimum wavelength/s with the highest difference between the normal and HCC groups; fifthly, the column and row mean for each spectral image were calculated and followed by computing of the RMSE between both target group consequently, the spectral response for each target group was revealed (b) Demonstration of the output results described in each step for determining the spectrum responses, till the highest RMSE.

### 3. Results

#### 3.1. Spectral cube image processing and computing spatial mean

To compute *spectral images spatial mean*, many steps have been followed, firstly, we have used Eqs. (1) and (2) (using our custom algorithm) for calibration and noise removal of the obtained spectral cube images (*Calibration + Noise removal using a moving average filter*). Consequently, the optimum wavelength wavelength/s with the highest difference between the normal and HCC groups have been processed by selecting thirteen frames concatenated normal images for HCC group and 13 concatenated images for normal groups covering the entire wavelengths as depicted in [Figure 4a], high attenuation of the light with a low transmission; has been observed with HCC samples, compared to the normal samples that shown; low attenuation of light and high transmission. The next step is the evaluation of the light transmission rate from the cross bonding images for selecting the discrimination optimal wavelength between different groups; by using Eqs. (3), (4), (5), (6), and (7) for calculation the row and column mean for each spectrum image. Solving Eqs. (3), (4), (5), (6), and (7); represents the amount of transmitted and scattered light of image pixel as shown in [Figure 4b and c], The amount of scattered light for normal have shown higher intensity than HCC samples for both column and row mean. Furthermore, the

spectral patterns for the normal sample showed relatively higher intensity (transmission) than the HCC sample in the wavelength ranged between 400 and 1000 nm. For precisely, indentifying and confirming the wavelength with maximum difference between the two groups, the Root Mean Square Error (RMSE), which is the *standard deviation* of the *prediction errors* that measure how column and/or row mean of normal samples are far from the column and/or row mean of the abnormal samples. The RMSE has been calculated for the 26 concatenated images shown in [Figure 4a] using Eqs. (8) and (9); which has increased gradually till maximum at 600 nm, and then decreased gradually till 1000 nm. Moreover, RMSE was significantly high (more than 100) between 500nm and 700nm for both row mean and column mean which refer to the spectral response of both samples [Figures 4d & 3b].

#### 3.2. Spectral signature algorithm for the cube image

Finally, after resolving the maximum differences of the wavelength ranges between the two group; their Spectral signatures have been revealed, by computing the average of the spatial mean (column + row mean) for the entire spectral images (128 frames) from 400 to 1000nm with 5nm resolution, using Eq. (10). Consequently, the optimum wavelength for discrimination between different groups; has been allocated precisely.

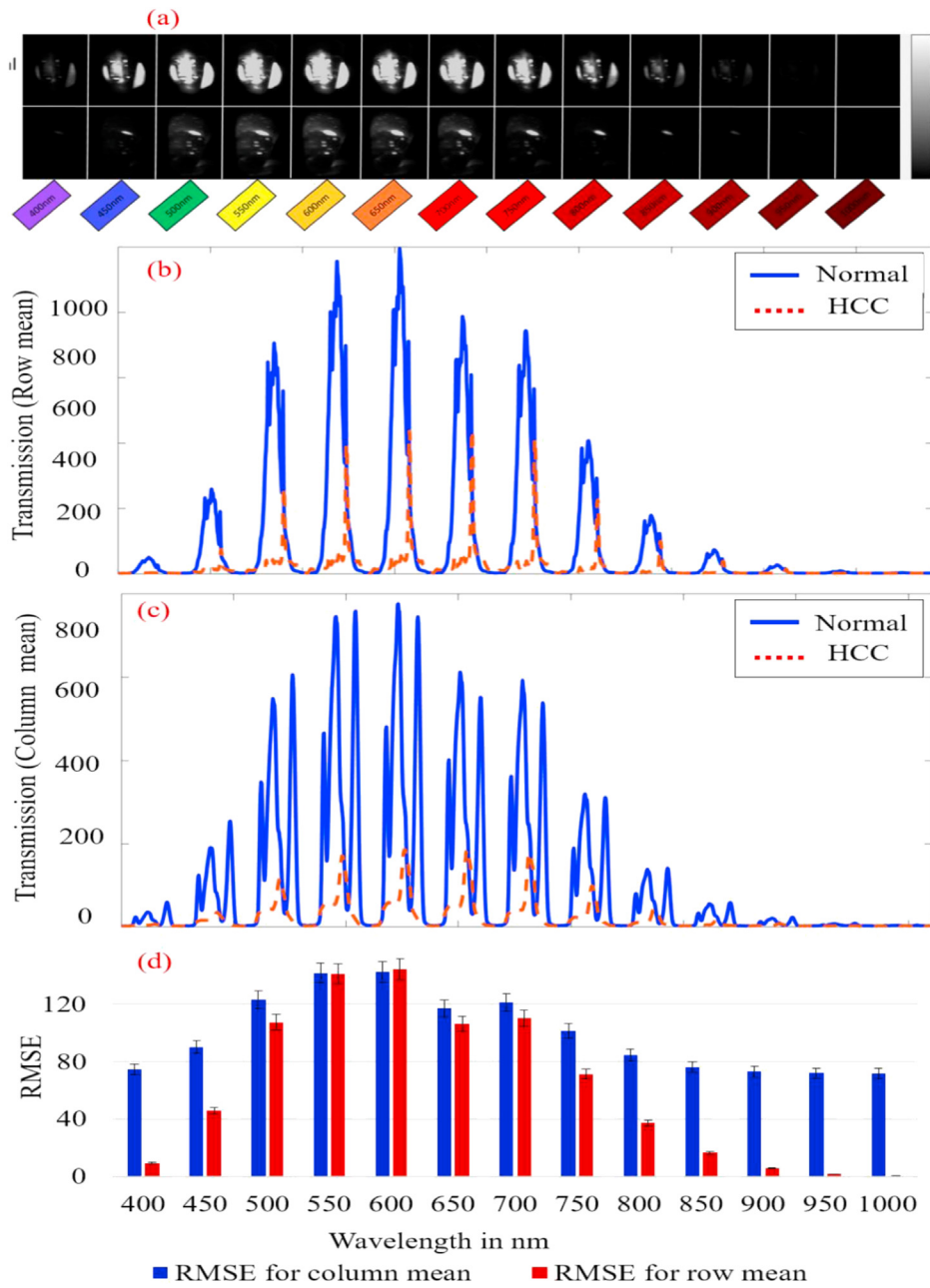


**Figure 4.** The spectrum response for both normal and HCC samples; (a) Spectral images for the total RNA sera samples (13 normal concatenated images in the top +13 HCC concatenated images in the bottom) at different wavelengths (400nm:1000nm). The intensity differences between each target group are distinguishable in each the images at various wavelengths; (b) Row means for the spectrum images which represent the amount of transmitted and scattered light of image pixel (Normal samples in solid-blue lines and HCC samples in red-dash lines); (c) Column means for the spectrum images which represent the amount of transmitted and scattered light of image pixel (Normal samples in solid-blue lines and HCC samples in red-dash lines); (d) RMSE between all normal and HCC samples along the y (row mean) and x (column mean) dimensions.

### 3.3. Spectral signature normalization and cross-correlation

The whole algorithm steps for actuary determining the specific spectral signature for each group, within the obtained optimum discrimination wavelength (*accurately calculated spatial mean*) is shown in [Figure 5a]. Normalization has been done for neutralization of spectral signature amplitude. The accurate spectral signature obtained is shown in [Figure 5b].

In the same context, a cross-correlation is a matrix; where, each cell is showing the correlation coefficient between the spectral signature concerning reference samples ( $\bar{I}_r$ ), normal samples ( $\bar{I}_n$ ), and HCC samples ( $\bar{I}_h$ ). Eqs. (11), (12), (13), (14), and (15) have been followed for correlation coefficient calculations:

$$(Z_r)_i = \left( \left( \bar{I}_r \right)_i - \mu_{\bar{I}_r} \right) / \sigma_{\bar{I}_r} \tag{11}$$

$$(Z_n)_i = \left( \left( \bar{I}_n \right)_i - \mu_{\bar{I}_n} \right) / \sigma_{\bar{I}_n} \tag{12}$$

$$(Z_h)_i = \left( \left( \bar{I}_h \right)_i - \mu_{\bar{I}_h} \right) / \sigma_{\bar{I}_h} \tag{13}$$

Where:

$(\mu_{\bar{I}_r})$ ,  $(\mu_{\bar{I}_n})$ , and  $(\mu_{\bar{I}_h})$  are the mean values of  $(\bar{I}_r)$ ,  $(\bar{I}_n)$ , and  $(\bar{I}_h)$  respectively.

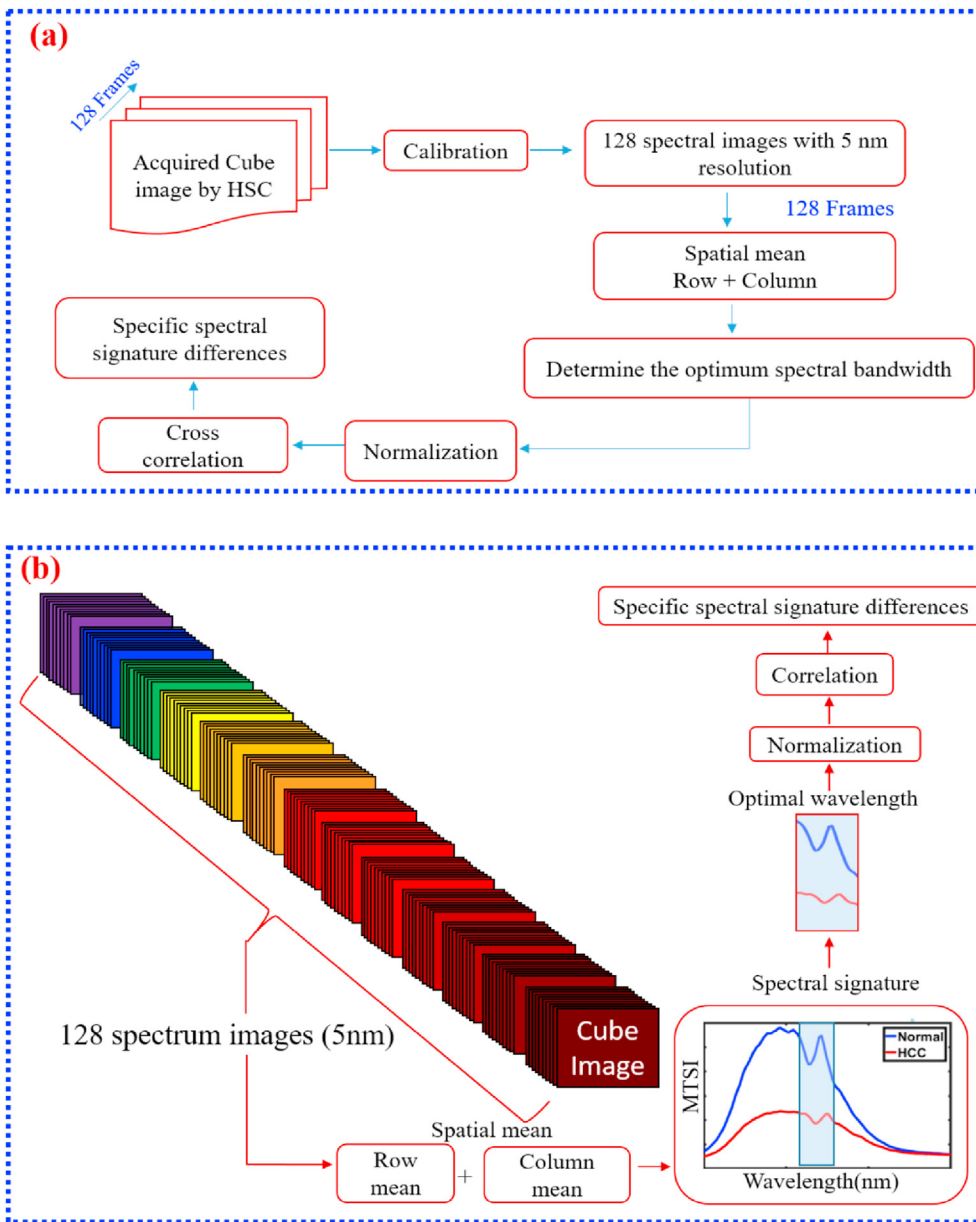


**Figure 5.** The image processing protocol for the Specific spectral signature differences allocation between the HCC and normal in RNA sera samples. (a) A flowchart for the acquired cube image to present each step in extraction of the specific spectral signature differences for HCC and normal samples which starts firstly by acquiring the cube image by the HSC, secondly by cube image calibration for artifacts and electronic noise impacts whipping out; (b): Demonstration of the expected output results in each step in Extraction of the specific spectral signature differences for each target group.

$(\sigma_{\bar{I}_r})$ ,  $(\sigma_{\bar{I}_n})$  and  $(\sigma_{\bar{I}_h})$  are the standard deviations of  $(\bar{I}_r)$ ,  $(\bar{I}_n)$ , and  $(\bar{I}_h)$  respectively.

$$R_n = \left( \frac{1}{N-1} \sum_{i=1}^N (Z_r Z_n)_i \right) = \frac{(Z_r Z_n)_1 + (Z_r Z_n)_2 + \dots + (Z_r Z_n)_N}{N-1} \tag{14}$$

$$R_h = \left( \frac{1}{N-1} \sum_{i=1}^N (Z_r Z_h)_i \right) = \frac{(Z_r Z_h)_1 + (Z_r Z_h)_2 + \dots + (Z_r Z_h)_N}{N-1} \tag{15}$$

Where:

$(R_n)$  is the correlation coefficient for the normal samples.  
 $(R_h)$  is the correlation coefficient for the HCC samples.

Table 2 shows how the correlation coefficient for the normal and HCC samples has been achieved for precisely revealing the accurate and specific spectral signatures.

Each cell represents the cross correlation coefficient between the row and the column. Calculations have been done according to Eqs. (11), (12), (13), (14), and (15) (cross correlation coefficient algorithm). As shown in the table, column 1 represents the cross correlation coefficient between the reference, normal and HCC samples, which produced negative correlation with the normal and positive correlation with the HCC samples. Moreover, each column such as column 2 showing the correlation between Normal sample 1 and all the other samples and so on for all the columns. The net result is that the normal samples are positively correlated with each other and negatively correlated with the HCC samples and vice versa. This indicates that there is statistically similarity between the negative samples together and the HCC samples together, and difference between normal and HCC samples.

**Table 2.** Correlation matrix showing the correlation between the spectral signature of the reference ( $\bar{I}_r$ ), normal ( $\bar{I}_n$ ), and HCC samples respectively.

Groups	Ref.	Normal 1	Normal 2	Normal 3	Normal 4	Normal 5	HCC 1	HCC 2	HCC 3	HCC 4	HCC 5
Ref.	1										
Normal 1	-0.3108	1									
Normal 2	-0.3761	0.98812	1								
Normal 83	-0.4861	0.65536	0.75788	1							
Normal 4	-0.6081	0.90601	0.9528	0.85742	1						
Normal 5	-0.5524	0.95582	0.97943	0.78053	0.98731	1					
HCC 1	0.9131	-0.4171	-0.5146	-0.7641	-0.7337	-0.6513	1				
HCC 2	0.97176	-0.339	-0.4265	-0.6423	-0.6643	-0.5879	0.98121	1			
HCC 3	0.93528	-0.379	-0.4754	-0.7241	-0.7049	-0.6216	0.99724	0.99141	1		
HCC 4	0.97418	-0.4281	-0.5047	-0.6511	-0.7214	-0.6593	0.97574	0.99315	0.98285	1	
HCC 5	0.3971	-0.0659	-0.2009	-0.7638	-0.3848	-0.2526	0.69381	0.59042	0.67206	0.53179	1

3.4. Spectral signature of clinical samples

Figure 6a shows the whole spectrum using HSI for all the selected groups, with obvious spectral signatures differences between them, which allow their characterization, identification, and classification within 3 min. Interestingly, the benign samples have shown spectral signature in the same amplitude with the HCC samples but with same normal signature. Also, all the HCC samples have completely different signature at the optimum wavelength than the other groups, even sample HCC 5 which has higher amplitude than the other HCC samples, and have the same signature of HCC. According to the clinical data, the BCLC stage (A2, which is early stage HCC), and its AFP level is 20 ng/ml, which confirms that the tumor is still in its early stage, that's why we speculate the high amplitude of this sample and in the same time having the same HCC spectral signature.

Moreover [Figure 6b], shows the amplitude normalized spectral signature within the optimum wavelength red band (633–700 nm), of the clinical samples in Figure 6a. Normalization has been done to confirm the unique spectral pattern for each sample of the different groups. These results agreed with Duan et al. who reported that the spectral signature of the liver tumor was distinguishable from that of the normal tissue at 600–900 nm wavelength [50]. Duan et al, has done HSI on liver normal tissues and HCC tissues, and his data revealed that the tumor liver tissues has shown a significant reflection peak at 700 nm at the red band, with no band for the normal tissues at this wavelength. Accordingly, as our work is on RNA extracted from the HCC and normal subjects, our obtained spectral signature is around the area obtained by Duan et al. Moreover, Oranit, B., et al [51], has classified the HCC using Hyperspectral imaging on histopathological images, and he concluded that the green spectrum has the highest classification with 99.8%, and the red spectrum with 98.34%, which is not significant difference in addition, the authors

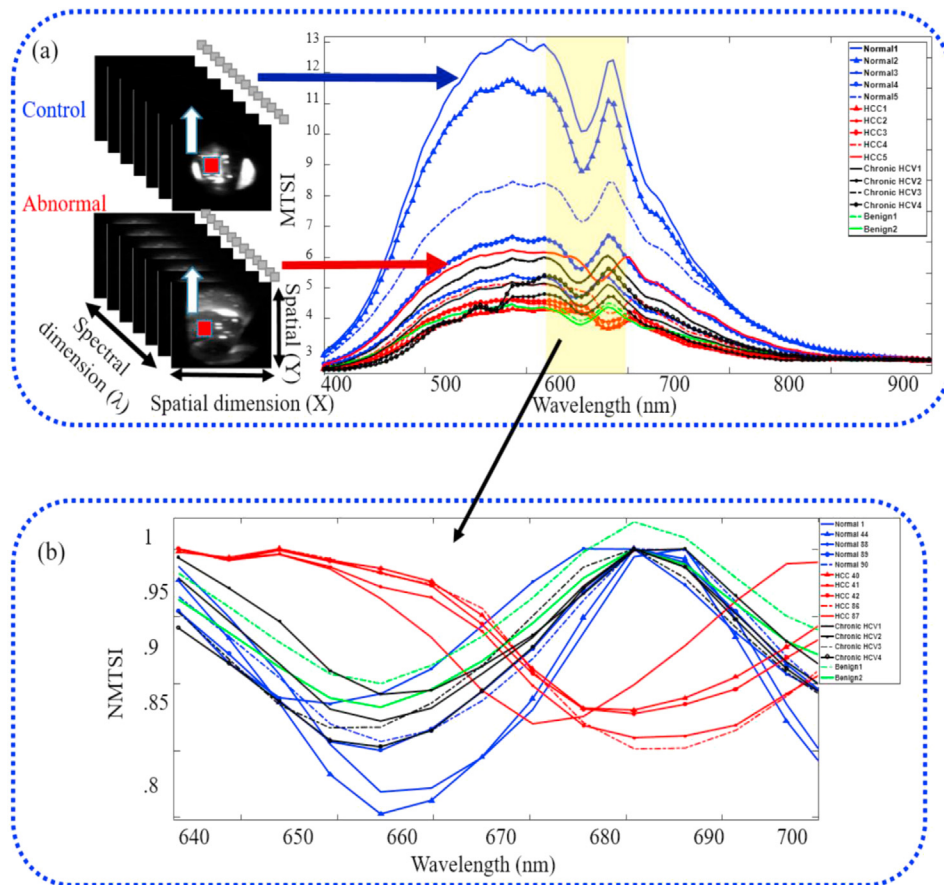


**Figure 6.** Spectrum signatures for Control and abnormal samples (Normal samples in blue lines, HCC samples in red lines, Chronic HCV in black lines, and Benign samples in green lines); (a) Spectral signatures are produced by averaging (Spatial mean x,y) the cube image through the entire wavelength (5nm resolution); the horizontal axis shows the different wavelengths in nanometers and the vertical axis shows the mean of transmission spectral images (MTSI); (b) Normalized spectral signatures that show the optimum wavelength (633nm:700nm) to differentiate between normal and HCC samples; the horizontal axis shows the different wavelengths in nanometers and the vertical axis shows the normalized mean of transmission spectral images (NMTSI).

declared that the five colors used in the study have similar classification performance. Taking together these data performed on liver tissues and histopathological images using HSI, with the signature obtained in this study, that is in the red band is confirmation that our generated signature is significantly related to the HCC; taking into consideration that we have analyzed total RNA extracted from normal and HCC samples, neither tissues nor histopathological images, and that extracted RNA is related to liver cancer.

### 3.5. Cross correlation and spectral shift of the normalized spectral signature

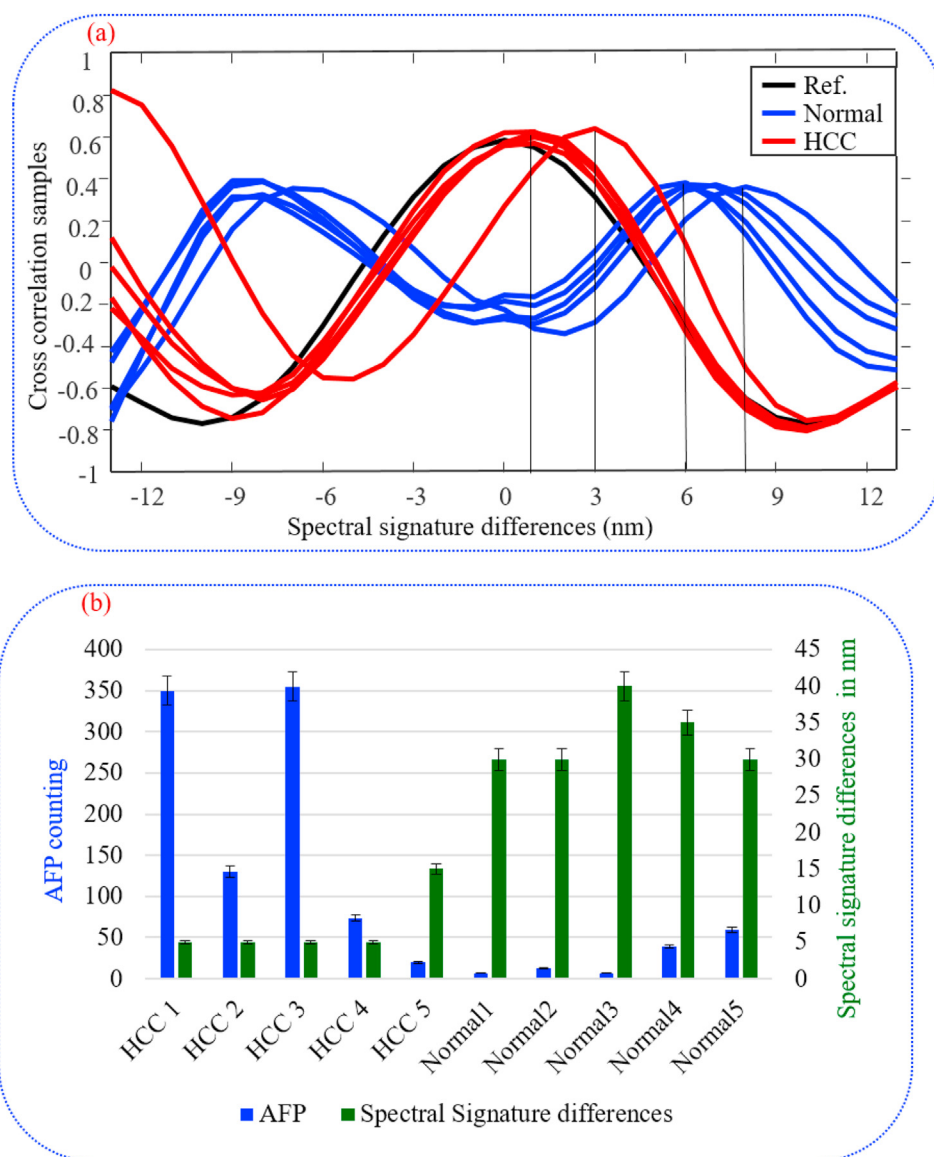
To determine the spectral signature shift (difference in the wavelength pattern), between the different samples, cross-correlation of the normalized spectral signature that obtained at the red band (633–700 nm) has been implemented with respect to the reference as shown in [Figure 7a]. The spectral signatures shift between the normal group and the reference are ranged from 30 to 40 nm; while the difference between the HCC group and reference ranged from 5 to 15 nm. That means a significant difference between the normal and HCC samples compared to the reference, that confirms the unique pattern and hence, the specific spectral signature for each group.

To ensure the integrity of the data obtained, a comparison between the HCC gold standard biomarker, the AFP level, and the spectral signatures differences for each sample, has been performed. As shown in [Figure 7b], significant relation between the AFP level and the spectral shift has been observed; which is in concordance with the AFP level between samples, with the exception of one HCC sample 5, which has a higher spectral shift than the other HCC samples. This sample has low level of AFP (20 ng/ml), and its BCLC stage of A2 (early HCC stage). Interestingly, normal samples 4 and 5 have a higher level of AFP than HCC sample 5; and at the same time; their spectral signal differences are much higher than the HCC sample 5. This confirmed that the spectral signature is highly specific and is superior to the AFP level, even if the AFP is low, the HCC could be determined by our generated specific spectral signature. Consequently, the spectral signature could be used as a sensitive early prognostic marker for HCC, even in the very early stage of HCC.

### 3.6. Expression of serum RNA cancer panel in HCC and healthy control

The RNA serum panel expression has been done for all the samples in the study. We have selected different types of RNA (mRNA, LncRNAs, miRNAs) with differential expression levels between the normal and HCC

**Figure 7.** Spectral signature differences between normal and HCC samples within the red-band (633–700 nm); (a) Spectral shift calculated using cross-correlation algorithm with respect to the reference sample, where normal and HCC samples are in blue and red lines respectively, and reference sample in black line; the horizontal axis shows the different wavelengths in nanometers and the vertical axis shows the cross-correlation samples; (b) Spectral signature shift (in green bars) compared to AFP counting (in blue bars). As shown, as the AFP level decreases the spectral shift increases and vice versa.



groups, as another confirmation step at a molecular level. In HCC sera samples, *miRNA 23a-3p*, *miRNA 221-3p*, and *miRNA 106b-3p*, in addition to, the transcripts *FOXM1 mRNA*, *MCM6 mRNA*, and *LAT1 mRNA*, expression were at a level higher than that of the healthy control. Moreover, LncRNAs RNAs, (*lncRNA-WRAP53*, *LncRNA-CTBP1-AS*, and *lncRNA-RP11-513115*) expression profile in HCC were higher than the normal healthy control. On the other hand, sera HCC samples have shown lower expression of *ATG12* and *STAT1 mRNA* compared with control. These data are in full agreement and well established as expression profile panel for HCC in cells and serum; as described in details in the discussion section [Figure 8].

### 3.7. Heating effect on spectral signature behavior of RNA samples

The heating effect on the spectral signatures of normal and HCC samples behavior have been studied using a commercial laser source (650nm) as an illumination system, and the data was acquired using a Hyperspectral camera. The effect of heating and cooling on the RNA samples has a significant effect on RNA folding (spatial organization),

and the refolding behavior (Figure 9). This is a key experiment in this pilot study, and the data obtained are highly crucial for proving that light interaction behavior is affected by the RNA molecules spatial organization (RNA folding), and hence, the spectral signature. As shown in [Figure 9], when the cancer samples were heated, and then cooled no significant effect has been observed in their spectral signature, which is attributed to their less compact structure (RNA folding is somehow wobbly) as we proposed. On the other hand, a significant change in the normal samples has been observed after heating/cooling procedures. The spectral signature of the normal samples after denaturation (heating) and then cooled to room temperature; their spectral signature has approached the HCC signature; which means that the RNA in the normal were more compact due to their dense folding structure, and has been affected by heating and refold into smaller or compact structure, making its interaction with the light behaves like the HCC samples. Interestingly, the samples were analyzed at wavelength 650 nm which is in agreement with the spectral signature that has been generated; and it is known that no absorbance for the nucleic acids at this wavelength.

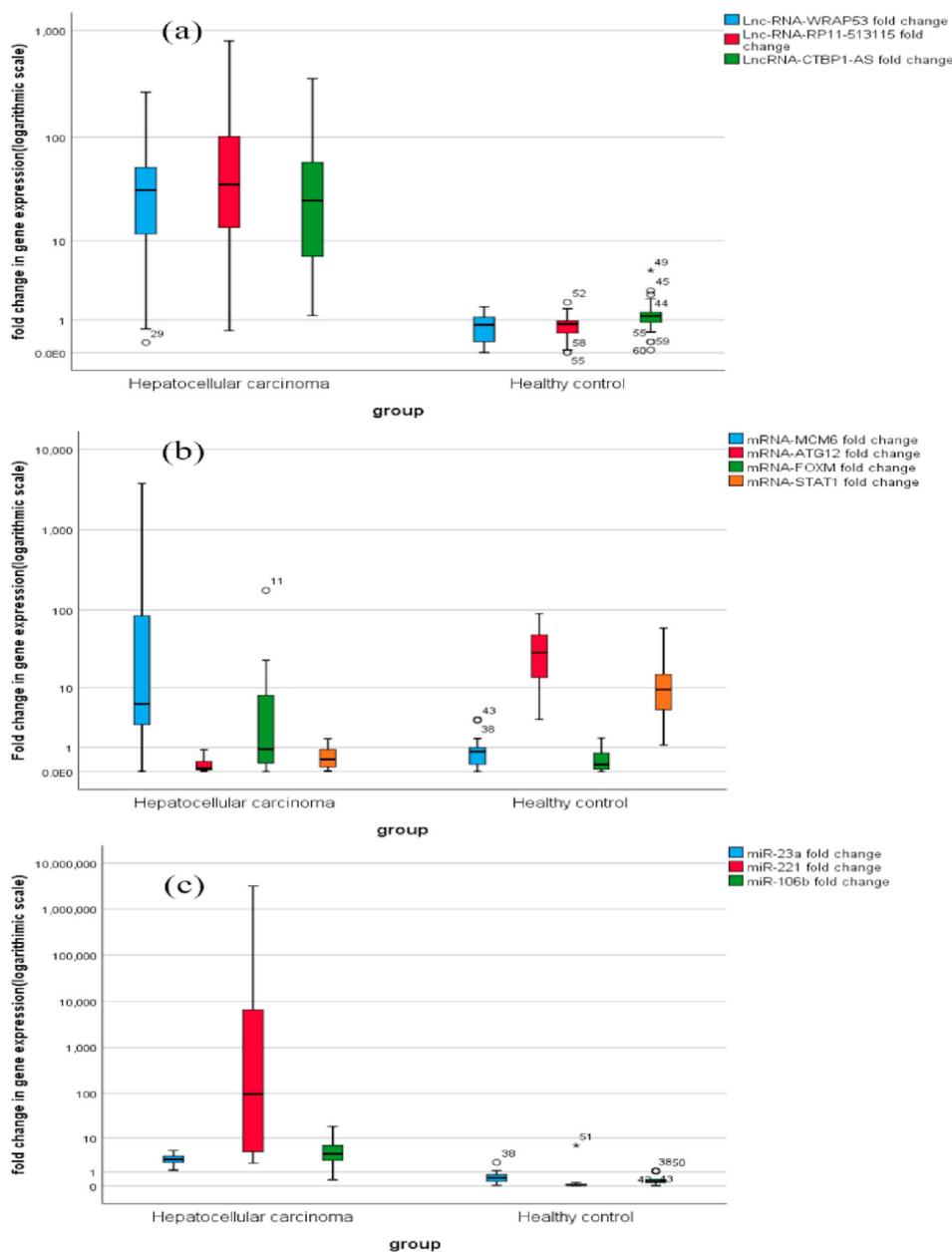


**Figure 8.** BOXPLOT represents serum RNA cancer panel expression as determined by qRT-PCR between all the HCC and healthy control groups in this study. The data expressed as fold change in gene expression ( $P < 0.05$ ). (a) LncRNAs, (b) mRNAs and (c) mi-RNAs. The expression profiles of the selected RNAs of different types are in concordance with the Hepatocellular carcinoma expression profile. The line inside the box is the median. The top and bottom lines of the box are the first and third quartiles, respectively. The top and bottom whiskers are the 5th and 95th percentiles, respectively.

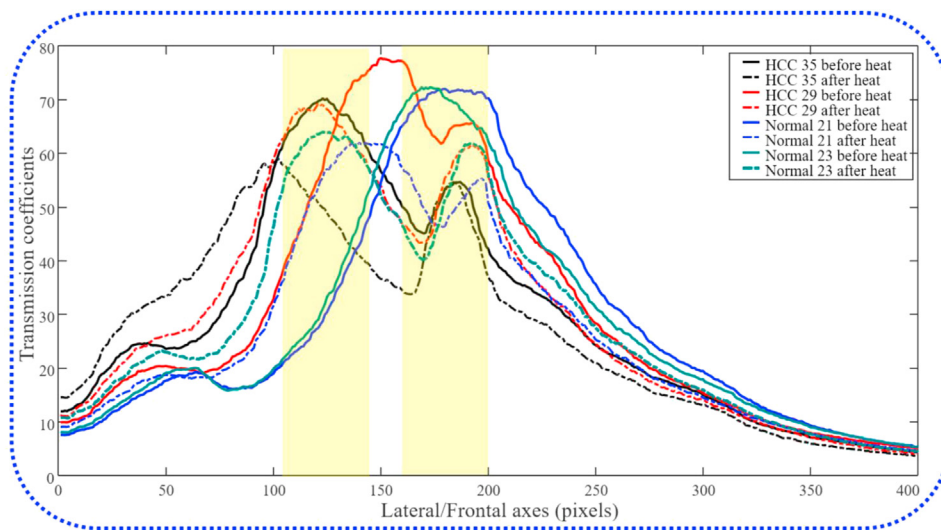


**Figure 9.** Spectral signatures variation with heat effect: Spectral signatures when using laser pointer (650nm) with a Hyperspectral camera; Normal samples before heating in solid blue line and solid green line and after heating in-dash blue line and dash green line; the horizontal axis shows the different lateral/frontal axes in pixels and the vertical axis shows the transmission coefficients (attenuation and scattering values); HCC samples before heating in solid red line and solid black line and after heating in-dash blue line and dash green line, The data was acquired using a Hyperspectral camera. All normal samples in dash lines have distinct signatures that differ from HCC spectral signature in solid lines.

### 3.8. Laser pointer and CCD camera

Further data were acquired using the custom simple setup shown in [Figure 10a], which consists of a CCD mobile phone camera instead of the Hyperspectral camera and a commercial laser pointer (650nm) as an illumination system. This experiment aims to produce a simple, affordable, and cheap detection technique [Figure 10b]. is showing, the

spectral signatures for both groups using the simple setup, which is almost the same signature obtained when using HSI shown in Figure 9.

### 4. Discussion

Hepatocellular carcinoma is a complex disease. The progress in the transcriptome analysis has paved the way to understand HCC

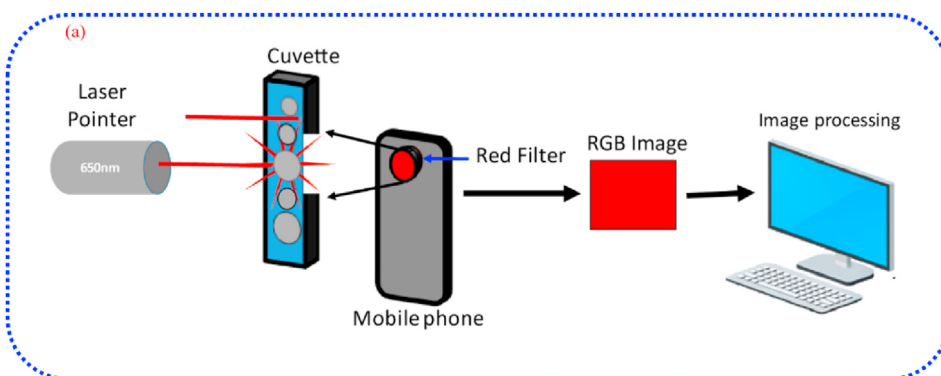
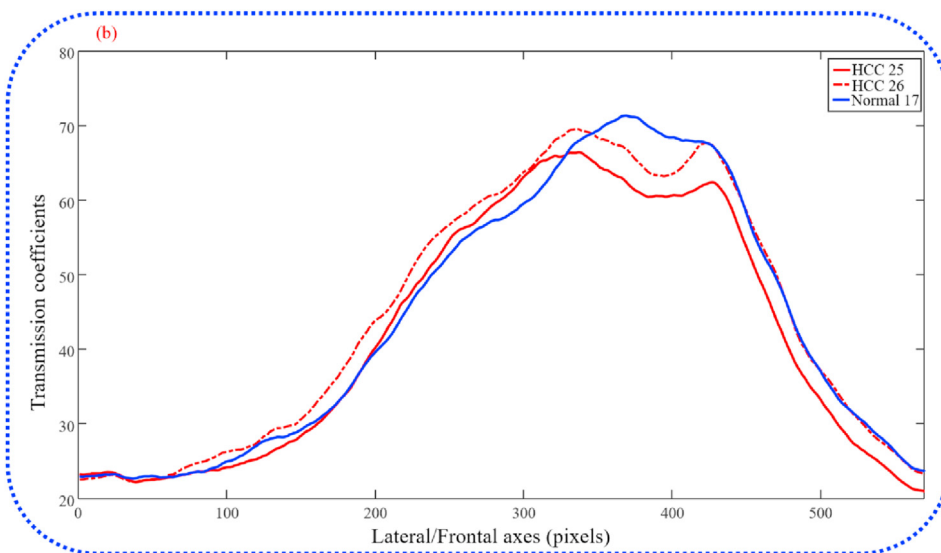


**Figure 10.** A simple, low-cost optical imaging biosensor: (a) A remote, cheap, and simple biosensor have been developed for HCC detection by hardware and software processing. The biosensor comprising a low cost red laser pointer (650nm) along with Smartphone CCD mobile camera; which acquires distinctive RBG images for the HCC, and the normal groups; (b) The spectral signatures of normal and HCC samples which indicate the differences between the two groups (Normal and HCC) when using a commercial laser pointer (650nm) as an illumination system and a Smartphone CCD mobile camera. Normal sample in blue lines have distinct signatures that differ from HCC spectral signature in red lines. The horizontal axis shows the different lateral/frontal axes in pixels and the vertical axis shows the scattering values.



development at a molecular level that discloses many pathways; and documented by many researchers [15, 31, 52]. Currently, clinical diagnostics professionals are heading for liquid biopsies seeking specific RNAs as early non-invasive detection of cancer including HCC. Many panels based on circulating RNAs and/or RNAs within circulating extracellular vesicles, and circulating tumor cells nucleic acids cargo have been studied which is based mainly on their differential expression aiming an early specific and sensitive cancer prognosis and diagnosis.

In this pilot study, we have retrieved a panel of genes related to HCC pathogenesis and implicated in different molecular pathways linked to carcinogenesis [Figure 8]. shows the Real-Time PCR results for the selected genes panel. The **cell cycle-related transcripts** *MCM6 mRNA* [53, 54], *FOXM1 mRNA* [55, 56], are up regulated and down regulated in the HCC and control groups respectively, while the, **apoptosis, and immune checkpoint regulation:** *STAT1 mRNA* [57, 58], *LAT1 mRNA* [59, 60] and **autophagy:** *ATG12 mRNA* [61, 62] are down regulated and up regulated in the HCC and normal groups respectively (Figure 8b).. Furthermore, we have selected miRNA 23a-3 [63,64,65], miRNA 221-3p [66,67], and miRNA 106b-3p [68,69], based on computation prediction that they are the epigenetic regulators of the chosen mRNAs, and their deregulation in HCC as reported in previous literature. Their pathway enrichment analysis revealed that the chosen miRNA is linked to PI3K-Akt signaling pathway, Jak-STAT signaling pathway and Chemokine signaling pathway (miR-23a-3p), p53 signaling pathway, and cell cycle signaling (miR-221-3p and miR-106b-3p), and they are all up regulated in the HCC group (Figure 8c). Finally, the 3 Long non-coding RNAs (*lncRNA-WRAP53*), (*lncRNA-CTBP1-AS*), and (*lncRNA-RP11-513115*) [70–73] are linked to HCC; and they up regulated in the HCC group compared to the control group (Figure 8a). These lncRNAs are targeting and interacting with either the chosen miRNAs or mRNAs. Briefly, there is a significant differential expression pattern in the chosen RNA cancer panel between HCC and control groups; which proof that the extracted RNA from the different samples are falling between either the HCC or normal samples. This experiment was done as a molecular evidence for the total RNA extracted origin.

These differential expressions of the different groups are in agreement with the obtained spectral signatures that were observed by HSI.

Herein, an advanced data acquisition algorithm with cube image processing techniques has employed using a Custom optical imaging system for the discrimination between normal, cirrhotic, and HCV chronic infected patients and HCC using total RNA extracted from sera. HSI is a potential tool in medical diagnostics with many applications in discriminating between cancer and non-cancerous tissues, sensing and detecting the abnormal lesions. We have recently exploit the HIS in developing custom optical imaging system for diagnosis and imaging of ex-vivo breast cancer [74, 75], in addition to, using HIS in liver tissue characterization for liver thermal ablation [76]. However, to the best of our knowledge, this is the first study to use a Hyperspectral camera in producing distinctive spectral signatures based on total RNA extracted from sera samples.

The difference or evolving of genetic alterations in cancer cells compared to the normal cells, one of the main causes of developing cancer. This could be explained by the accumulation of aberrant RNA differential expression rate pattern in the cancer cells. Also, the RNA Binding Proteins (RBPs), which plays a major role in temporal and spatial organization of RNA in the cell, mutated RBPs are significantly influencing the final RNAs expression. Moreover, the small size of the cytoplasm, and organelles, the aberrant splicing, loss of polarity of cytoskeleton, adhesion molecules (stickiness), with poorly defined tumor boundaries, and overall loss of normal cell specialized cell features, with immature differentiation of cancer cell, high rate of cell division, results in the presence of RNAs (coding and non-coding), with many mutations and inappropriate spatial organization, and affecting RNA stability thus, affecting the final RNA folding (tertiary structure) [19, 77, 78, 79].

Minimum free energy achievement is the key required for RNA tertiary structure stabilization. The stability and the dynamics of the native

RNA tertiary structure depend mainly on minute changes in the base sequence. Additionally, as mentioned above cellular proteins as RBPs affect the folding rate and its pathway.

Therefore, we hypothesize that in cancer cells, the dipole-dipole and RNA molecules staking are loose and not highly stable due to their imbalance and high rate of mutations that prevent the establishment of the native RNA folding in normal cells. Consequently, the spatial organization (folding) of the different nucleic acids including RNA molecules is changed.

A compact folding structure of RNAs has been observed in this study as shown in Figure 4a, where the normal samples have higher reflectance (scattering) than the cancer samples, which indicates the high condensed structure of the normal RNA other than the cancer samples. This could be explained by the well-known factors governing predicting size by scattering; which is: *i) wavelength of the incident radiation, ii) refractive index, and iii) scattering angle*. All these three factors in our system were constant and so, the variation in the reflectance/scattering obtained was due to the **size difference between the different groups**, which is mainly the RNA tertiary structure (Folding behavior). This could be explained; that the photon energy dissipates in the RNA of cancer samples due to its primary loose structure with immature spatial organization.

Moreover, the RMSE for both the column and row mean has been calculated, and as shown in Figures 3a and 4d, the highest difference between the two groups was found between 500 and 700 nm leading to narrowing the spectral signature difference. Interestingly, these data are in concordance with, Akabri et al [43], that found the cancer tissues have low intensity in a wavelength range between 450-950 nm, and also, with the reflectance/scattering behavior shown in Figure 4a.

As shown in Figure 6a, the spectral signatures within 400nm–600 nm for the HCC group have the same pattern and normal sample amplitudes in most samples exceeded HCC samples. In the same context, the two benign samples have shown the same signature as the normal subjects; however, with a lower amplitude than the HCC sample. The benign tumors approach the HCC in the amplitude, but with the same signature of the normal samples. Moreover, the four samples with chronic HCV infection and no HCC have shown the same spectral signature as the normal control, with lower amplitude, with the only cirrhotic sample and chronic HCV infection, with higher amplitude. These obtained data confirm our hypothesis that differential expression of different RNAs and their spatial organization (folding) plays a great role in the obtained spectral signature, and hence; the disease stage, and ensures our findings Figure 6a. Also, spectral signatures within 633nm–700nm for normal samples had a distinct pattern than that of the HCC samples which were so obvious with normalized spectral signatures within 633nm–700 nm normalization of the obtained spectral signature Figure 6b.

To ensure the integrity of the data obtained, a comparison between the AFP level (the HCC gold standard biomarker, and the spectral signatures shift differences from the reference for each sample, has been done as shown in Figure 7b, after calculating the spectral shift between the samples in Figure 7a. A direct correlation has been found between the level of AFP and the spectral shift signature which is in concordance with the proposed HCC detection method, with the AFP as an HCC biomarker. Interestingly, sample HCC 5, with BCLC stage A2 i.e. at an early stage with no portal hypertension, has shown higher spectral shift (approach the normal but having the signature of HCC) in addition to, low AFP level compared to the other HCC samples with higher cancer stages. In the same context, normal samples 4 and 5 have a higher level of AFP than HCC 5; their spectral signal differences are much higher than the HCC sample 5. This confirmed that the spectral signature is highly specific and sensitive and could differentiate HCC at a very early stage.

The heating effect to proof our RNA folding hypothesis are shown in Figure 9 in which; Normal samples before heating have a distinct signature pattern that lies between 160 and 200 on the spatial domain (lateral/frontal axis- X-axis) which differs from HCC spectral signature pattern that lies between 105 and 145 spatial domain. After heating; the normal spectral signature pattern has been changed significantly with

and lies between 105 and 145 on the spatial domain (lateral/frontal axis) and approaches that of the HCC spectral signature before heating. On the other hand, heating HCC samples did not affect the spatial domain significantly, and the samples have been slightly shifting to the left, with the same signature pattern. This could be attributed to the high condensed structure of the normal RNA samples, which on heating and then cooling the RNA refolds in less compact structure, and approach the HCC RNA folding which is already, less folded, (tertiary structure is not accurately folded as the normal RNA samples).

These data confirmed that the differential expression and hence the spatial organization of RNA are the key players in the obtained specific spectral signatures.

We have utilized the cumulative data obtained and analyzed in this pilot study to build a simple system based on the laser pointer and mobile CCD camera for total RNA based HCC diagnosis, the system is shown in Figure 10a. By using a laser pointer in the red band, and acquire the images by the mobile CCD camera, data analyzed using the same algorithms, and spectral signature for the normal and HCC samples are shown in Figure 10b. The horizontal axis shows the different lateral/frontal axes in pixels and the vertical axis shows the scattering values; each group has a distinct pattern and can be easily and specifically differentiated from each other in less than 2 min using such custom simple, setup, mobile camera, and commercial laser pointer.

## 5. Conclusion and future prospective

A custom optical imaging system using HSI has been established for the first time to detect HCC utilizing a specific spectral signature for circulating total RNA with high accuracy, sensitivity, specificity, and short time turnover.

High speed, a high-resolution Hyperspectral camera captured the change in Transcriptomes structure by determination of its optical properties after multispectral light source sample interaction, the results demonstrate the capability to discriminate between normal, benign, cirrhotic, and HCC samples which agreed with PCR, biochemical, and tumor staging data for the investigated samples.

Moreover, we have exploited the spectral signatures obtained in building a simple, affordable, and cheap system based on the commercial laser pointer and mobile CCD camera. To the best of our knowledge, we are the first to determine the optimum wavelength for circulating RNA dependent HCC diagnosis and using a simple system for remote sensing of HCC specifically and cancer in general. This will open the door for incorporating machine learning with our proposed system that could be used in cancer early detection and infectious diseases.

## Declarations

### Author contribution statement

Sherif M. Shawky, Ibrahim H. Aboughaleb, Marwa Matboli, Yasser H. El-Sharkawy: Conceived and designed the experiments; Performed the experiments; Analyzed and interpreted the data; Contributed reagents, materials, analysis tools or data; Wrote the paper.

### Funding statement

This work was supported by the Military Technical College (2018\_1), Cairo, Egypt.

### Data availability statement

Data will be made available on request.

### Declarations of interest statement

The authors declare no conflict of interest.

## Additional information

No additional information is available for this paper.

## Acknowledgements

Aboughaleb IH has carried out data collection, study design, and system development, and validation in clinical samples, manuscript drafting, performed experiments, and analyzed data, Marwa Matboli shared in study design, samples collection, Performing Molecular Biology experiments and statistics, processing approval of the revised draft, Shawky SM shared in study design, performing Molecular Biology Experiments and statistics, data analysis and interpretation, writing and processing approval of the revised draft, EL-Sharkawy YH the system development, shared in study design, data analysis and approval of the revised draft.

## References

- [1] WHO. Hepatitis [cited June 2020]; Available from: <https://www.who.int/health-topics/hepatitis>, 2019.
- [2] F. Bray, et al., Global cancer statistics 2018: GLOBOCAN estimates of incidence and mortality worldwide for 36 cancers in 185 countries, *CA A Cancer J. Clin.* 68 (6) (2018) 394–424.
- [3] WHO, WHO Calls for Better Monitoring of Viral Hepatitis and Liver Cancer, 2018 [cited 2020 June 2020]; Available from: <https://www.who.int/hepatitis/news-events/hepatitis-surveillance-protocol-story/en/>.
- [4] WHO. Hepatitis B, Fact sheet, Available from: <https://www.who.int/news-room/fact-sheets/detail/hepatitis-b>, 2019 February 2020.
- [5] WHO. Hepatitis C Fact Sheets, 2019 [cited 2020 February 2020]; Available from: <https://www.who.int/news-room/fact-sheets/detail/hepatitis-c>.
- [6] WHO. Cancer, Key Facts, 2019 [cited July 2020]; Available from: <https://www.who.int/news-room/fact-sheets/detail/cancer>.
- [7] H. Mani, D.E. Kleiner, Liver biopsy findings in chronic hepatitis B, *Hepatology* 49 (S5) (2009) S61–S71.
- [8] F.P. Russo, et al., When and how should we perform a biopsy for HCC in patients with liver cirrhosis in 2018? A review, *Dig. Liver Dis.* 50 (7) (2018) 640–646.
- [9] A. Doyle, M. Sherman, Liver biopsy for hepatocellular carcinoma (HCC): should this be a routine? *Current Hepatology Reports* 16 (1) (2017) 46–50.
- [10] J.A. Marrero, et al., Diagnosis, staging, and management of hepatocellular carcinoma: 2018 practice guidance by the American association for the study of liver diseases, *Hepatology* 68 (2) (2018) 723–750.
- [11] Peter R. Galle, Alejandro Forner, Josep M. Llovet, Vincenzo Mazzaferro, Fabio Piscaglia, Jean-Luc Raoul, Peter Schirmacher, Valérie Vilgrain, et al., European Association for the Study of the Liver: Management of hepatocellular carcinoma, *J. Hepatol.* 69 (1) (2018) 182–236. Epub 2018 Apr 5. Erratum in: *J Hepatol.* 2019 Apr;70(4):817. PMID: 29628281.
- [12] J.K. Heimbach, et al., AASLD guidelines for the treatment of hepatocellular carcinoma, *Hepatology* 67 (1) (2018) 358–380.
- [13] S.H.B. Do Seon Song, Changes of guidelines diagnosing hepatocellular carcinoma during the last ten-year period, *Clin. Mol. Hepatol.* 18 (3) (2012) 258.
- [14] V.V. Tchatalbachev, et al., Seeding of the rectus sheath with hepatocellular carcinoma after image guided percutaneous liver biopsy using coaxial biopsy needle system, *J. Radiol. Case Rep.* 9 (1) (2015) 18–25.
- [15] X. Bisteau, et al., The complex relationship between liver cancer and the cell cycle: a story of multiple regulations, *Cancers* 6 (1) (2014) cancers6010079 [pii] 10.3390/cancers6010079, 79–111.
- [16] P.A. Farazi, R.A. DePinho, Hepatocellular carcinoma pathogenesis: from genes to environment, *Nat. Rev. Canc.* 6 (9) (2006) nrc1934 [pii] 10.1038/nrc1934, 674–687.
- [17] C. Cha, R.P. Dematteo, Molecular mechanisms in hepatocellular carcinoma development, *Best Pract. Res. Clin. Gastroenterol.* 19 (1) (2005) S1521–6918 (04) 00174-X [pii]10.1016/j.bpg.2004.11.005, 25–37.
- [18] A.I.a.C., C. Baba, Comparative Oncology. 2010/09/01, The Publishing House of the Romanian Academy, 2007, 47.
- [19] H.D. Yang, S.W. Nam, Pathogenic diversity of RNA variants and RNA variation-associated factors in cancer development, *Exp. Mol. Med.* 52 (4) (2020) 582–593.
- [20] J.H. Xu, et al., The mRNA, miRNA and lncRNA networks in hepatocellular carcinoma: an integrative transcriptomic analysis from Gene Expression Omnibus, *Mol. Med. Rep.* 17 (5) (2018) 6472–6482.
- [21] J.U. Marquardt, et al., Sequential transcriptome analysis of human liver cancer indicates late stage acquisition of malignant traits, *J. Hepatol.* 60 (2) (2014) 346–353.
- [22] D.T. Ross, et al., Systematic variation in gene expression patterns in human cancer cell lines, *Nat. Genet.* 24 (3) (2000) 227–235.
- [23] J.B. Welsh, et al., Analysis of gene expression profiles in normal and neoplastic ovarian tissue samples identifies candidate molecular markers of epithelial ovarian cancer, *Proc. Natl. Acad. Sci. Unit. States Am.* 98 (3) (2001) 1176–1181.

- [24] L.-M. Li, et al., Serum microRNA profiles serve as novel biomarkers for HBV infection and diagnosis of HBV-positive hepatocarcinoma, *Canc. Res.* 70 (23) (2010) 9798–9807.
- [25] R. Yao, et al., Prospect of circular RNA in hepatocellular carcinoma: a novel potential biomarker and therapeutic target, *Frontiers in oncology* 8 (2018).
- [26] S.C. Anna, et al., Emerging roles of long non-coding RNA in cancer, *Canc. Sci.* 109 (7) (2018) 2093–2100.
- [27] B. Lei, et al., Circular RNA: a novel biomarker and therapeutic target for human cancers, *Int. J. Med. Sci.* 16 (2) (2019) 292–301.
- [28] M.M. Kamel, et al., Investigation of long noncoding RNAs expression profile as potential serum biomarkers in patients with hepatocellular carcinoma, *Transl. Res.* (2016) 168134–168145.
- [29] L.-L. Chen, The biogenesis and emerging roles of circular RNAs, *Nat. Rev. Mol. Cell Biol.* 17 (4) (2016) 205.
- [30] R. Chen, et al., Exosomes in hepatocellular carcinoma: a new horizon, *Cell Commun. Signal.* 17 (1) (2019) 1.
- [31] A. Alqahtani, et al., Hepatocellular carcinoma: molecular mechanisms and targeted therapies, *Medicina (Kaunas)* 55 (9) (2019) medicina55090526.
- [32] L. Eldridge, P.D. Cancer, Cells vs. Normal cells: how are they different? *Cancer* (2019 December 07), 2019 [3/March/2020]; Available from: <https://www.verywellhealth.com/cancer-cells-vs-normal-cells-2248794>.
- [33] S.H. Lee, et al., Liquid Biopsy in Hepatocellular Carcinoma. 2020/02/21, in: *Hepatocellular Carcinoma: Translational Precision Medicine Approaches*, Springer Nature Switzerland AG, 2019.
- [34] X. Wang, et al., Extracellular mRNA detected by molecular beacons in tethered lipoplex nanoparticles for diagnosis of human hepatocellular carcinoma, *PLoS One* 13 (6) (2018).
- [35] C. Han, et al., Regulation of microRNAs function by circular RNAs in human cancer, *Oncotarget* 8 (38) (2017) 64622–64637.
- [36] P.-O. Gaudreau, et al., The present and future of biomarkers in prostate cancer: proteomics, genomics, and immunology advancements, *Biomarkers Canc.* 8 (2016) 15–33.
- [37] G.C. Tseng, et al., Investigating multi-cancer biomarkers and their cross-predictability in the expression profiles of multiple cancer types, *Biomark. Insights* 4 (2009) 57–79.
- [38] A. Solovoyov, et al., Global cancer transcriptome quantifies repeat element polarization between immunotherapy responsive and T cell suppressive classes, *Cell Rep.* 23 (2) (2018). S2211–1247.
- [39] A. Robles-Kelly, C.P. Huynh, *Imaging Spectroscopy for Scene Analysis*, Springer Science & Business Media, 2012.
- [40] A.F.H. Goetz, Three decades of hyperspectral remote sensing of the Earth: a personal view, *Remote Sens. Environ.* 113 (2009) S5–S16.
- [41] F. Pierna, et al., Chemometrics in NIR hyperspectral imaging: theory and applications in the agricultural crops and products sector, in: *Reference Module in Chemistry, Molecular Sciences and Chemical Engineering*, Elsevier, 2020.
- [42] H. Akbari, et al., Cancer detection using infrared hyperspectral imaging, *Canc. Sci.* 102 (4) (2011) 852–857.
- [43] H. Akbari, et al., Hyperspectral imaging and quantitative analysis for prostate cancer detection, *J. Biomed. Optic.* 17 (7) (2012).
- [44] S.W. Chan, et al., Breast tumor detection and classification using intravoxel incoherent motion hyperspectral imaging techniques, *BioMed Res. Int.* 2019 (2019) 3843295.
- [45] L. Gao, R.T. Smith, Optical hyperspectral imaging in microscopy and spectroscopy - a review of data acquisition, *J. Biophot.* 8 (6) (2015) 441–456.
- [46] A.M. Siddiqi, et al., Use of hyperspectral imaging to distinguish normal, precancerous, and cancerous cells, *Cancer* 114 (1) (2008) 13–21.
- [47] A.O. Gerstner, Early detection in head and neck cancer - current state and future perspectives, *GMS Curr. Top. Otorhinolaryngol., Head Neck Surg.* (2008) 7Doc06.
- [48] Y. Khouj, et al., Hyperspectral imaging and K-means classification for histologic evaluation of ductal carcinoma in situ, *Front Oncol* 8 (2018) 17.
- [49] C.H. Jun, et al., Barcelona clinic liver cancer-stage C hepatocellular carcinoma: a novel approach to subclassification and treatment, *Medicine (Baltim.)* 96 (17) (2017) 10.
- [50] F. Duan, et al., Feasibility of hyperspectral analysis for discrimination of rabbit liver VX2 tumor, *World J. Gastrointest. Oncol.* 11 (1) (2019) 1.
- [51] B. Oranit, et al., Multispectral band Analysis: application on the classification of hepatocellular carcinoma cells in high-magnification histopathological images, *J. Cytol. Histol.* (2015) 2015.
- [52] J.U. Marquardt, et al., Sequential transcriptome analysis of human liver cancer indicates late stage acquisition of malignant traits, *J. Hepatol.* 60 (2) (2014) 346–353.
- [53] X. Liao, et al., Distinct diagnostic and prognostic values of minichromosome maintenance gene expression in patients with hepatocellular carcinoma, *J. Canc.* 9 (13) (2018) 2357–2373.
- [54] Y. Chen, et al., A direct interaction between P53-binding protein 1 and minichromosome maintenance complex in HepG2 cells, *Cell. Physiol. Biochem.* 47 (6) (2018) 2350–2359.
- [55] J.C. Wei, et al., Sorafenib inhibits proliferation and invasion of human hepatocellular carcinoma cells via up-regulation of p53 and suppressing FoxM1, *Acta Pharmacol. Sin.* 36 (2) (2015) 241–251.
- [56] T. Zhang, et al., KIAA0101 is a novel transcriptional target of FoxM1 and is involved in the regulation of hepatocellular carcinoma microvascular invasion by regulating epithelial-mesenchymal transition, *J. Canc.* 10 (15) (2019) 3501–3516.
- [57] B. Mitra, et al., Hepatitis B virus precore protein p22 inhibits alpha interferon signaling by blocking STAT nuclear translocation, *J. Virol.* 93 (13) (2019).
- [58] B. Ma, et al., Dichotomous functions of phosphorylated and unphosphorylated STAT1 in hepatocellular carcinoma, *J. Mol. Med. (Berl.)* 97 (1) (2019) 77–88.
- [59] M. Namikawa, et al., Expression of amino acid transporters (LAT1, ASCT2 and xCT) as clinical significance in hepatocellular carcinoma, *Hepatol. Res.* 45 (9) (2015) 1014–1022.
- [60] J. Li, et al., The impact of L-type amino acid transporter 1 (LAT1) in human hepatocellular carcinoma, *Tumour Biol* 34 (5) (2013) 2977–2981.
- [61] H. Wei, et al., Long noncoding RNA HAGLROS promotes cell proliferation, inhibits apoptosis and enhances autophagy via regulating miR-5095/ATG12 axis in hepatocellular carcinoma cells, *Int. Immunopharm.* 73 (2019) S1567–S5769.
- [62] M. Shen, L. Lin, Functional variants of autophagy-related genes are associated with the development of hepatocellular carcinoma, *Life Sci.* 235 (19) (2019) S0024–3205.
- [63] L. Bao, et al., Correlation between miR-23a and onset of hepatocellular carcinoma, *Clin Res Hepatol Gastroenterol* 38 (3) (2014) S2210–7401.
- [64] Y. Liu, et al., Adipose-derived exosomes deliver miR-23a/b to regulate tumor growth in hepatocellular cancer by targeting the VHL/HIF axis, *J. Physiol. Biochem.* 75 (3) (2019) 391–401.
- [65] Y. Yan, et al., MicroRNA-23a downregulates the expression of interferon regulatory factor-1 in hepatocellular carcinoma cells, *Oncol. Rep.* 36 (2) (2016) 633–640.
- [66] O. Shaker, et al., miRNA-101-1 and miRNA-221 expressions and their polymorphisms as biomarkers for early diagnosis of hepatocellular carcinoma, *Infect. Genet. Evol.* 51 (17) (2017). S1567–1348.
- [67] F. Chen, et al., Clinical potential of miRNA-221 as a novel prognostic biomarker for hepatocellular carcinoma, *Canc. Biomarkers* 18 (2) (2017) CBM161671.
- [68] H.S. Yen, et al., miR-106b promotes cancer progression in hepatitis B virus-associated hepatocellular carcinoma, *World J. Gastroenterol.* 22 (22) (2016) 5183–5192.
- [69] H.E.A. Ali, et al., Circulating miR-26a, miR-106b, miR-107 and miR-133b stratify hepatocellular carcinoma patients according to their response to transarterial chemoembolization, *Clin. Biochem.* 65 (2019) S0009–9120.
- [70] M.M. Kamel, et al., Investigation of long noncoding RNAs expression profile as potential serum biomarkers in patients with hepatocellular carcinoma, *Transl. Res.* 168 (15) (2016) S1931–5244.
- [71] A.H. El-Tawdi, et al., Evaluation of circulatory RNA-based biomarker panel in hepatocellular carcinoma, *Mol. Diagn. Ther.* 20 (3) (2016) 265–277.
- [72] M. Matboli, et al., Pantoprazole attenuates tumorigenesis via inhibition of exosomal secretion in a rat model of hepatic precancerous lesion induced by diethylnitrosamine and 2-acetamidofluorene, *J. Cell. Biochem.* 120 (9) (2019).
- [73] A. Abd El Gwad, et al., Role of exosomal competing endogenous RNA in patients with hepatocellular carcinoma, *J. Cell. Biochem.* 119 (10) (2018) 8600–8610.
- [74] I.H. Aboughaleb, et al., Hyperspectral imaging for diagnosis and detection of ex-vivo breast cancer, *Photodiagnosis Photodyn. Ther.* 31 (2020). S1572–1000.
- [75] M.H. Aref, et al., Custom optical imaging system for ex-vivo breast cancer detection based on spectral signature, *Surg Oncol* 35 (2020) S0960–7404.
- [76] M.H. Aref, et al., Tissue characterization utilizing hyperspectral imaging for liver thermal ablation, *Photodiagnosis Photodyn. Ther.* 31 (2020) 101899.
- [77] L. Coppin, et al., Messenger RNA life-cycle in cancer cells: emerging role of conventional and non-conventional RNA-binding proteins? *Int. J. Mol. Sci.* 19 (3) (2018), ijms19030650.
- [78] K.C. Martin, A. Ephrussi, mRNA localization: gene expression in the spatial dimension, *Cell* 136 (4) (2009).
- [79] I. Barbieri, T. Kouzarides, Role of RNA modifications in cancer, *Nat. Rev. Canc.* 20 (6) (2020).